Evaluation of turbulence models in MHD channel and square duct flows

R. Chaudhary, B. G. Thomas and S. P. Vanka

Department of Mechanical Science & Engineering
University of Illinois at Urbana-Champaign
Urbana, IL, USA

ABSTRACT

In this paper, several low and high Reynolds number versions of k-ε and Reynolds stress turbulence models have been evaluated in a channel and a square duct flow with and without a magnetic field by comparing the predictions with direct numerical simulations data. The simulations are performed using FLUENT solver. The additional source terms for magnetic field effects on turbulence have been included through user-defined functions. A systematic assessment of the predicted mean flow, turbulence quantities, frictional losses and computational costs of the various turbulence models is presented.

All the models predict mean axial velocity reasonably well, but the predictions of turbulence parameters are less accurate. Velocity predictions are worse for the square duct flow due to secondary flows generated by the turbulence. The implementation of the MHD sources generally improves predictions in MHD flows, especially for low-Re k-ε models. The high-Re models using the wall treatments show little improvement, perhaps due to the lack of MHD effects in the wall formulations. Finally, at low Reynolds numbers, the Lam-Bremhorst (LB) low-Re k-ε model was found to give better predictions than other models for both hydrodynamic and magnetic field influenced turbulent flows.

1. INTRODUCTION

Reynolds-Averaged Navier-Stokes (RANS) simulations are widely used to optimize various industrial flows because of their low computational cost. However, it is well-known that their accuracy in complex flows is limited by the difficulties in modeling the complex turbulence interactions through transport equations for the mean flow variables [1]. Significant effort has already been devoted to validation, improvement, and custom tailoring of these models of turbulent flows for different classes of flows [2-8]. This is usually done through comparisons with experimental data. However, with the availability of Direct Numerical Simulation (DNS) and Large Eddy Simulation (LES) computed flow fields, it has also become possible to evaluate the turbulence models using DNS / LES data [2, 9-11].

Despite the importance of magnetic fields in material processing, very limited work [12-15] exists on improving and testing turbulence models to include the effects of a magnetic field on the turbulence. A few modified models with magnetic field effects have been tested in channel flow/rectangular duct flow with a partial magnetic field (low-Re k-ε and Reynolds stress model (RSM)) [12-13], pipe flow (low-Re k-ε) [14] and free surface channel flow (k-ε) [15]. The modifications proposed in the latter two of these studies (pipe flow [14] and free surface channel flow [15]) were based upon bulk properties of the flow and cannot be generalized to other flows. The first two studies (k-ε and RSM, [12-13]) relate the magnetic field generated source terms in the turbulent transport equations to the local properties, and therefore can be generalized to other flows. However, these models have been so far tested only in a turbulent channel flow and in a rectangular duct with a partial magnetic field. For the rectangular duct with a partial magnetic field only the mean velocity was compared. The mean velocity obtained with this model was reported to show better agreement with measurements but no comparisons are available for turbulence quantities [12].

The present work reports a systematic assessment of a number of turbulence models, and their variants, for magnetohydrodynamic (MHD) flow in two representative geometries: a) channel flow, and b) a square duct flow. Confined internal flows through long pipes and ducts are relevant in many commercial flows. The square duct flow is more complicated to predict because of the turbulence-driven secondary flows [16]. The various models considered are: a) 3 variants of high-Re two-equation models (Standard k-ε (SKE) [17], RNG k-ε (RNG) [18], Realizable k-ε (RKE) [19], b) 6 low-Re k-ε models (Abid [20], Lam-Bremhorst (LB) [21], Launder-Sharma (LS) [22], Yang-Shih (YS) [23], Abe-Kondoh-Nagano (AKN) [24], and Chang-Hsieh-Chen (CHC) [25-26]) and c) 2 second-momentum closure Reynolds Stress Models with Linear Pressure Strain (RSM-LPS) and Stress-Omega (RSM-Sω) [27-31]) models along with standard wall functions (SWF) [32], non-equilibrium wall functions (NEWF) [33], or two-layer wall treatment combined with single-blended wall function (enhanced wall treatment or EWT) [34-35, 30]. The simulations have been performed using FLUENT [30] and the effect of magnetic field on turbulence, as given by Kenjereš and Hanjalić [12-13], has been incorporated through additional source terms using user-defined functions (UDF). Mean velocities, turbulent kinetic energy (TKE), root mean square (RMS) of velocity fluctuations, MHD sources/sinks and frictional losses are compared against available DNS data in channel and square duct flows.

2. TURBULENCE MODELS TESTED

The ensemble averaged Navier-Stokes equations are solved [36-37]:

$$\frac{\partial \overline{u}_i}{\partial t}+\frac{\partial \overline{u}_i\overline{u}_j}{\partial x_j}=-\frac{1}{\rho}\frac{\partial \overline{p}}{\partial x_i}+\frac{\partial}{\partial x_j}\left(\nu\frac{\partial \overline{u}_i}{\partial x_j}\right)+\frac{\partial R_{ij}}{\partial x_j}+\overline{F}_L \tag{1}$$

where, $R_{ij}=-\overline{u_i'u_j'}$: Reynolds Stresses, and $\overline{F}_L$ is the average Lorentz force due to magnetic field. The k-ε models use the Boussinesq hypothesis for Reynolds stresses (i.e. $R_{ij}=-\overline{u_i'u_j'}=\nu_t\left(\frac{\partial \overline{u}_i}{\partial x_j}+\frac{\partial \overline{u}_j}{\partial x_i}\right)-\frac{2}{3}k\delta_{ij}$). The base equations for the two equation k-ε models are:

$$\frac{\partial \rho k}{\partial t}+\frac{\partial}{\partial x_k}\left(\rho\overline{u}_k k\right)=\frac{\partial}{\partial x_j}\left[\left(A\right)\frac{\partial k}{\partial x_j}\right]+G_k-\rho\varepsilon+\rho D \tag{2}$$

$$\frac{\partial \rho \varepsilon}{\partial t}+\frac{\partial}{\partial x_k}\left(\rho\overline{u}_k \varepsilon\right)=\frac{\partial}{\partial x_j}\left[\left(B\right)\frac{\partial \varepsilon}{\partial x_j}\right]+C+\rho E \tag{3}$$

Where, $k=\overline{u_i'u_i'}/2$, $\varepsilon=\nu\overline{\frac{\partial u_i'}{\partial x_j}\frac{\partial u_i'}{\partial x_j}}$, and $G_k=-\rho\overline{u_i'u_j'}\frac{\partial \overline{u}_j}{\partial x_i}$

After defining A, B, C, D and E in the above equations for each k-ε model and the basic equations for RSM, modifications for the presence of a magnetic field are described.

2.1. Standard k-ε model (SKE)

In this classic model [17], A, B, C, D and E in Eqs. 2-3 are given as follows;

$$A=\mu+\frac{\mu_t}{\sigma_k},\ B=\mu+\frac{\mu_t}{\sigma_\varepsilon},\ C=C_{\varepsilon 1}\frac{\varepsilon}{k}G_k-\rho C_{\varepsilon 2}\frac{\varepsilon^2}{k},\ D=0,\ E=0 \tag{4}$$

$\mu_t=\rho C_\mu k^2/\varepsilon$, $C_\mu=0.09$, $C_{\varepsilon 1}=1.44$, $C_{\varepsilon 2}=1.92$, $\sigma_k=1.0$, $\sigma_\varepsilon=1.3$,.

2.2. RNG k-ε model (RNG)

The RNG k-ε turbulence model [18] includes an additional term (R_ε) in the ε equation, and uses different turbulent Prandtl numbers, so A, B, C, D and E in this model are as follows:

$$A=\alpha_k\mu_{eff},\ B=\alpha_\varepsilon\mu_{eff},\ C=C_{\varepsilon 1}\frac{\varepsilon}{k}G_k-\rho C_{\varepsilon 2}\frac{\varepsilon^2}{k}-R_\varepsilon,\ D=0,\ E=0 \tag{5}$$

where, $\mu_{eff}=\mu+\mu_t$, $C_{\varepsilon 1}=1.42$, $C_{\varepsilon 2}=1.68$.

The inverse Prandtl numbers (α_k and α_ε) are calculated using formula derived from RNG theory,

$$\left|\left(\alpha-1.3929\right)/\left(\alpha_o-1.3929\right)\right|^{0.6321}\left|\left(\alpha+2.3929\right)/\left(\alpha_o+2.3929\right)\right|^{0.3679}=\mu/\mu_{eff},\ \alpha_o=1 \tag{6}$$

The additional term (R_ε) is defined as, $R_\varepsilon=\dfrac{C_\mu\rho\eta^3\left(1-\eta/\eta_0\right)}{1+\beta\eta^3}\dfrac{\varepsilon^2}{k},\ \eta=\dfrac{Sk}{\varepsilon}$ (7)

$$S=\sqrt{2s_{i,j}s_{i,j}},\ s_{i,j}=\frac{1}{2}\left(\frac{\partial\overline{u}_i}{\partial x_j}+\frac{\partial\overline{u}_j}{\partial x_i}\right),\ \eta_0=4.38,\beta=0.012$$

The differential formulation for effective viscosity for low-Re effects is defined as;

$$d\left(\left(\rho^2k\right)/\left(\sqrt{\varepsilon\mu}\right)\right)=1.72\left(\hat{\nu}/\sqrt{\hat{\nu}^3-1+C_\nu}\right)d\hat{\nu}\text{, where, }\hat{\nu}=\mu_{eff}/\mu\text{ and }C_\nu=100 \tag{8}$$

This equation can be integrated for $\hat{\nu}$ and the integration constant can be calculated under the condition that $\hat{\nu}=1,\text{when }k=0$.

2.3. Realizable k-ε model (RKE)

The RKE [19] has a realizable formulation to ensure positive normal Reynolds stresses and satisfy Schwarz inequality ($\overline{u'_a u'_b}^2\le\overline{u'^2_a}\,\overline{u'^2_b}$) in highly strained flows. This model has C_μ sensitized to the mean flow, k and ε. The new dissipation rate (ε) equation is derived from the exact mean-square vorticity fluctuation equation ($\varepsilon=\nu\overline{\omega_i\omega_i}$, $\omega_i=\partial u'_k/\partial x_j-\partial u'_j/\partial x_k$). The equations for $A,\ B,\ C,\ D$ and E in this model are as follows:

$$A=\mu+\frac{\mu_t}{\sigma_k},\ B=\mu+\frac{\mu_t}{\sigma_\varepsilon},\ C=\rho C_1S\varepsilon-\rho C_2\frac{\varepsilon^2}{k+\sqrt{\nu\varepsilon}},\ D=0,\ E=0 \tag{9}$$

$$C_2=1.9,\quad \sigma_k=1.0,\quad \sigma_\varepsilon=1.2,\ C_1=\max\left(0.43,\eta/\left(\eta+5\right)\right),\ \mu_t=\rho C_\mu k^2/\varepsilon$$

$$C_\mu=1/\left(A_0+A_s\left(kU^*/\varepsilon\right)\right),\text{ where }U^*=\sqrt{s_{i,j}s_{i,j}+\tilde{\Omega}_{i,j}\tilde{\Omega}_{i,j}},\ \tilde{\Omega}_{i,j}=\Omega_{i,j}-2\varepsilon_{ijk}\omega_k \tag{10}$$

$$,\ \bar{\Omega}_{i,j}=\frac{1}{2}\left(\frac{\partial\overline{u}_i}{\partial x_j}-\frac{\partial\overline{u}_j}{\partial x_i}\right),\ \varepsilon_{ijk}=\begin{cases}1 & \text{if(i, j, k) are cyclic}\\ -1 & \text{if(i, j, k) are anticyclic}\\ 0 & \text{otherwise}\end{cases}$$

with constants $A_0=4.04$ and $A_s=\sqrt{6}\cos\left(\phi\right)$, $\phi=\dfrac{1}{3}\cos^{-1}\left(\sqrt{6}W\right),\ W=\dfrac{s_{i,j}s_{j,k}s_{k,i}}{\tilde{S}^3},\ \tilde{S}=\sqrt{s_{i,j}s_{i,j}}$

2.4. Low-Re k-ε models

Six low-Re k-ε models [20-26] have been tested in the present work, with $A,\ B,$ and C defined in all of these models as follows:

$$A = \mu + \frac{\mu_t}{\sigma_k},\ \mu + \frac{\mu_t}{\sigma_\varepsilon},\ C = f_1 C_1 \frac{\varepsilon}{k} G_k - \rho f_2 C_2 \frac{\varepsilon^2}{k},\ \text{and}\ \mu_t = \rho f_\mu C_\mu k^2 / \varepsilon \tag{11}$$

The values of D and E, damping functions, wall boundary conditions and various constant for the different low-Re k-ε models are given in Table 1 and Table 2.

2.5. Reynolds stress model (RSM)

The exact transport equation for the six independent Reynolds stresses ($\overline{u_i' u_j'}$) in RSM can be written as [27-31]:

$$\frac{\partial}{\partial t}\left(\rho \overline{u_i' u_j'}\right) + \frac{\partial}{\partial x_k}\left(\rho \bar{u}_k \overline{u_i' u_j'}\right) = P_{ij} + D_{ij}^L + D_{ij}^T + \phi_{ij} - \varepsilon_{ij} \tag{12}$$

$P_{ij} = -\rho\left(\overline{u_i' u_k'} \frac{\partial \bar{u}_j}{\partial x_k} + \overline{u_j' u_k'} \frac{\partial \bar{u}_i}{\partial x_k}\right)$ (I: Production), $D_{ij}^L = \frac{\partial}{\partial x_k}\left(\mu \frac{\partial}{\partial x_k}\left(\overline{u_i' u_j'}\right)\right)$ (II: Molecular diffusion),

$D_{ij}^T = -\frac{\partial}{\partial x_k}\left(\rho \overline{u_i' u_j' u_k'} + \overline{p\left(\delta_{kj} u_i' + \delta_{ik} u_j'\right)}\right)$ (III: Turbulent diffusion), $\phi_{ij} = \overline{p\left(\frac{\partial u_i'}{\partial x_j} + \frac{\partial u_j'}{\partial x_i}\right)}$ (IV: Pressure strain), $\varepsilon_{ij} = 2\mu \overline{\frac{\partial u_i'}{\partial x_k} \frac{\partial u_j'}{\partial x_k}}$ (V: Dissipation), where $\delta_{ij} = 1$, if i=j, else 0.

Of these five terms, the last three (D_{ij}^T, ϕ_{ij} and ε_{ij},) require modeling, with the pressure strain (ϕ_{ij}) and dissipation (ε_{ij}) considered to be critical [28]. The turbulent diffusion term (i.e. D_{ij}^T, III) is modeled the same way as the molecular diffusion term [38]:

$$D_{ij}^T = \frac{\partial}{\partial x_k}\left(\frac{\mu_t}{\sigma_k} \frac{\partial}{\partial x_k}\left(\overline{u_i' u_j'}\right)\right), \text{ where } \mu_t = \rho C_\mu \frac{k^2}{\varepsilon},\ C_\mu = 0.09,\ \sigma_k = 0.82 \tag{13}$$

The dissipation tensor is defined from ε as: $\varepsilon_{ij} = (2/3)\delta_{ij}\rho\varepsilon$ (14)

The dissipation rate (i.e. ε) in the above equation is defined by same equations (with ($\sigma_\varepsilon = 1.0$)) as in SKE.

The main difference between RSM models is the handling of pressure strain (ϕ_{ij}) and many different ways have been proposed for high- and low- Re versions [27-28, 31, 39-41]. The current work tests low- and high-Re versions of the Linear Pressure Strain (LPS) model and low-Re stress omega model (RSM-Sω) formulations [30-31]. The high-Re version of LPS is used with SWF and NEWF. The low-Re version of LPS is used in conjunction with EWT.

In RSM-LPS, the pressure strain term is decomposed into three components,

$$\phi_{ij} = \phi_{ij1} + \phi_{ij2} + \phi_{ijw}, \phi_{ij1} = -C_1 \rho \frac{\varepsilon}{k}\left(\overline{u_i' u_j'} - \frac{2}{3}\delta_{ij} k\right), \phi_{ij2} = -C_2\left(\left(P_{ij} - C_{ij}\right) - \frac{2}{3}\delta_{ij}\left(\frac{P_{kk}}{2} - \frac{C_{kk}}{2}\right)\right) \quad (15)$$

where, $C_1 = 1.8$, $C_2 = 0.6$ and $C_{ij} = \frac{\partial}{\partial x_k}\left(\rho \bar{u}_k \overline{u_i' u_j'}\right)$ (convection term)

$$\begin{aligned} \phi_{ijw} &= C_1' \frac{\varepsilon}{k}\left(\overline{u_k' u_m'} n_k n_m \delta_{ij} - \frac{3}{2}\overline{u_i' u_k'} n_j n_k - \frac{3}{2}\overline{u_j' u_k'} n_i n_k\right)\frac{C_l k^{3/2}}{\varepsilon d} \\ &+ C_2'\left(\phi_{km2} n_k n_m \delta_{ij} - \frac{3}{2}\phi_{ik2} n_j n_k - \frac{3}{2}\phi_{jk2} n_i n_k\right)\frac{C_l k^{3/2}}{\varepsilon d} \end{aligned} \quad (16)$$

$C_1' = 0.5$, $C_2' = 0.3$, $C_l = C_\mu^{3/4}/\kappa$, $C_\mu = 0.09$, $\kappa = 0.42$, d is the normal distance to the wall. n_k is the x_k component of unit normal vector. In low-Re RSM-LPS with EWT, the constants (C_1, C_2, C_1' and C_2') are sensitized to Reynolds stress invariants and turbulent Reynolds number ($\mathrm{Re}_T = \rho k^2/\mu\varepsilon$) [41]. $C_1 = 1 + 2.58A\sqrt{A_2}\left(1 - \exp\left(-\left(0.0067\,\mathrm{Re}_T\right)^2\right)\right)$, $C_2 = 0.75\sqrt{A}$

, $C_1' = -(2/3)C_1 + 1.67$, $C_2' = \max\left(((2/3)C_2 - 1/6)/C_2, 0\right)$,

Where, $A = 1 - \frac{9}{8}\left(A_2 - A_3\right)$, $A_2 = a_{ik}a_{ki}$, $A_3 = a_{ik}a_{kj}a_{ji}$, $a_{ij} = -\left(-\rho\overline{u_i' u_j'} + (2/3)\rho k\delta_{ij}/\rho k\right)$

In addition to RSM-LPS, the RSM with low-Re stress omega formulation (RSM-Sω) was used for one low-Re non-MHD channel flow calculation. Details of this model are given in [30-31].

2.6. Near-Wall treatment

Near-wall treatment is very important in wall-bounded turbulent flows. Walls have high velocity gradients and thus are the main source of turbulence production. The wall regions are differently handled in different models. The low-Re models (i.e. Abid, LB, LS, YS, AKN, CHC, RSM-Sω with low Re-correction) use damping functions and need a fine grid to integrate up to viscous sublayer ($y^+ = yu_\tau/\nu(\tau_w = \rho u_\tau^2)$ <=1) [42]. The high-Re models (i.e. RKE, SKE, RNG, RSM etc.), use two different near-wall treatments [30-33]: i) wall functions which do not resolve the buffer region or viscous sublayer (applicable for 30< y^+ <300: SWF and NEWF), ii) two-layer model for ε and μ_t with a single blended law of wall for mean velocity (EWT). Formulations for the different wall treatment methods (SWF, NEWF and EWT) are given below.

2.6.1. Standard wall function (SWF)

The standard "law of the wall" for mean velocity [30, 32] is:

$$U^* = (1/\kappa)\ln(Ey^*),\ \kappa = 0.418,\ E = 9.79,\ C_\mu = 0.09 \tag{17}$$

Where, $U^* = U_p C_\mu^{1/4} k_p^{1/2} / (\tau_w / \rho)$, $y^* = \rho C_\mu^{1/4} k_p^{1/2} y_p / \mu$, (in equilibrium boundary layer y^* and y^+ are approximately equal) (subscript p stands for the cell center next to wall). U_p and k_p, and y_p are the TKE, tangential velocity and distanced of cell center from wall in the cell next to the wall respectively. τ_w is the wall shear stress.

At the wall, the normal derivative of TKE is taken zero (i.e. $\partial k / \partial n = 0$) and assuming rate of TKE production equal to rate of dissipation, the value of dissipation in the cell next to the wall can be calculated as, $\varepsilon_p = C_\mu^{3/4} k_p^{3/2} / (\kappa y_p)$

2.6.2. Non-equilibrium wall function (NEWF)

In this formulation, the log-law mean velocity of SWF is sensitized with pressure and a two layer approach for production and dissipation of turbulence is considered [30, 33].

$$\tilde{U} C_\mu^{1/4} k^{1/2} / (\tau_w / \rho) = (1/\kappa)\ln(E\rho C_\mu^{1/4} k^{1/2} y / \mu) \tag{18}$$

$$\tilde{U} = U - \frac{1}{2}\frac{\partial p}{\partial x}\left(\frac{y_v}{\rho\kappa\sqrt{k}}\ln\left(\frac{y}{y_v}\right) + \frac{y - y_v}{\rho\kappa\sqrt{k}} + \frac{y_v^2}{\mu}\right),\ y_v = \frac{\mu y_v^*}{\rho C_\mu^{1/4} k_p^{1/2}},\ y_v^* = 11.225.$$

y_v is viscous sublayer thickness. The two layer concept to calculate cell-average production (G_k) and dissipation rate (ε) is outlined below.

$$\tau_t = \begin{Bmatrix} 0, & y<y_v \\ \tau_w, & y>y_v \end{Bmatrix},\ k = \begin{Bmatrix} \left(\frac{y}{y_v}\right)^2 k_p, & y<y_v \\ k_p, & y>y_v \end{Bmatrix},\ \varepsilon = \begin{Bmatrix} \frac{2\nu k}{y^2}, & y<y_v \\ \frac{k^{3/2}}{C_l^* y}, & y>y_v \end{Bmatrix},\ C_l^* = \kappa C_\mu^{-3/4}$$

$$G_k = \frac{1}{y_n}\int_0^{y_n} \tau_t \frac{\partial U}{\partial y} dy = \frac{1}{\kappa y_n}\frac{\tau_w^2}{\rho C_\mu^{1/4} k_p^{1/2}}\ln\left(\frac{y_n}{y_v}\right), \text{ and } \varepsilon = \frac{1}{y_n}\int_0^{y_n} \varepsilon dy = \frac{1}{y_n}\left(\frac{2\nu}{y_v} + \frac{k_p^{1/2}}{C_l^*}\ln\left(\frac{y_n}{y_v}\right)\right)k_p$$

where, $y_n = 2y_p$. With G_k and ε, the TKE equation is solved in the domain with $\partial k / \partial n = 0$ at the wall.

2.6.3. Two-layer treatment with blended wall function (EWT)

This technique uses a two layer approach for eddy viscosity and dissipation rate based upon turbulent Reynolds number ($\mathrm{Re}_y = \rho\sqrt{k}y/\mu$, y is the normal distance from cell center to the wall) [30]. In the viscous region (i.e. $\mathrm{Re}_y < \mathrm{Re}_y^*$, $\mathrm{Re}_y^* = 200$), the momentum equation and TKE equations are solved as usual but the eddy viscosity and dissipation rates are calculated as:

$$\mu_{t,2} = \rho C_\mu l_\mu \sqrt{k},\ l_\mu = yC_l^*\left(1-\exp(-\mathrm{Re}_y/A_\mu)\right) \tag{19}$$

$\varepsilon = k^{3/2}/l_\varepsilon,\ l_\varepsilon = yC_l^*\left(1-\exp\left(-\mathrm{Re}_y/A_\varepsilon\right)\right)$, where $C_l^* = \kappa C_\mu^{-3/4},\ A_\mu = 70,\ A_\varepsilon = 2C_l^*$.

Further, the eddy viscosity of viscous region is blended with the fully turbulent viscosity to give smooth behavior in between viscous and fully turbulent regions:

$\mu_{t,enhanced} = \lambda_\varepsilon \mu_t + (1-\lambda_\varepsilon)\mu_{t,2}$ where, $\mu_t = \rho C_\mu k^2/\varepsilon$, $C_\mu = 0.09$. The same blending is performed for ε, where $\lambda_\varepsilon = 0.5\left(1+\tanh\left(\left(\mathrm{Re}_y - \mathrm{Re}_y^*\right)/A\right)\right)$, $A = \left|\Delta\mathrm{Re}_y/\tanh(0.98)\right|$, $\Delta\mathrm{Re}_y$ is assigned a value in between 5% to 20% of Re_y^* to give smooth behavior.

The blended single wall law is defined as [30, 34],

$$U^+ = e^\Gamma U^+_{\text{laminar}} + e^{1/\Gamma}U^+_{\text{turbulent}} \text{ and } dU^+/dy^+ = e^\Gamma dU^+_{\text{laminar}}/dy^+ + e^{1/\Gamma}dU^+_{\text{turbulent}}/dy^+ \tag{20}$$

$\Gamma = -a\left(y^+\right)^4/\left(1+by^+\right)$, $a = 0.01$, and $b = 5$. For turbulent region, the wall law with the effect of pressure is as follows [43-44]:

$$\frac{dU^+_{\text{turbulent}}}{dy^+} = \frac{1}{\kappa y^+}\left(S^{'}\right)^{1/2},\ S^{'} = \begin{Bmatrix} 1+\alpha y^+, & \mathrm{y}^+ < y_s^+ \\ 1+\alpha y_s^+, & \mathrm{y}^+ >= y_s^+ \end{Bmatrix},\ y_s^+ = 60, \text{ and } \alpha = \frac{\mu}{\rho^2 u_\tau^3}\frac{\partial p}{\partial x}$$

For laminar region, $dU^+_{\text{laminar}}/dy^+ = 1+\alpha y^+$. Eq. 2 is solved for TKE in the whole domain with $\partial k/\partial n = 0$ at the wall, and the G_k term in TKE equation is calculated using the velocity gradient (Eq-20) consistent with single wall law as given above.

2.6.4. Wall treatment in RSM model for Reynolds stresses

RSM model needs boundary conditions for Reynolds stresses in addition to the above wall treatment procedures. With SWF and NEWF, TKE is calculated using $k = 0.5\overline{u_i'u_i'}$ away from the wall and in the near wall cells, a transport equation, similar to as in SKE, for TKE (with $\sigma_k = 0.82$) is solved with $\partial k/\partial n = 0$ at the wall. Afterwards, the individual Reynolds

stresses are calculated using equation given below in near wall cells (derived based upon equilibrium of Reynolds stresses, i.e. production=dissipation) [30].

$$\overline{u_t'u_t'}/k = 1.098\,,\ \overline{u_\eta'u_\eta'}/k = 0.247\,,\ \overline{u_\lambda'u_\lambda'}/k = 0.655\,,\ -\overline{u_t'u_\eta'}/k = 0.255 \tag{21}$$

where subscripts t, η and λ stand for local tangential, normal and binormal coordinates respectively. With EWT, the normal derivatives of Reynolds stresses are zero at the wall.

2.7. MHD formulations

When the Magnetic Reynolds number, $\mathrm{Re}_m = vL(\mu\sigma)$, is <1 (such as for liquid metals), the induced magnetic field is negligible relative to the applied field. Based on Ohm's law and conservation of charge, coupled equations for electric potential, ϕ, and Lorentz force, $\vec{F}_L$ can be solved as follows [45, 30].

$$\nabla^2\phi = \nabla\cdot\left(\vec{v}\times\vec{B}_0\right) \text{ and } \vec{F}_L = \sigma\left(-\nabla\phi + \vec{v}\times\vec{B}_0\right)\times\vec{B}_0 \tag{22}$$

In time varying fields, and when the induced current is significant, (i.e. Re_m >1), the Maxwell's equations are combined with Ohm's law to obtain a transport equation for the induced magnetic field, $\vec{b}$ [45, 30].

$$\frac{\partial\vec{b}}{\partial t} + (\vec{v}\cdot\nabla)\vec{b} = \frac{1}{\mu\sigma}\nabla^2\vec{b} + \left(\left(\vec{B}_o + \vec{b}\right)\cdot\nabla\right)\vec{v} - (\vec{v}\cdot\nabla)\vec{B}_o - \frac{\partial\vec{B}_0}{\partial t} + \frac{1}{\mu\sigma}\nabla^2\vec{B}_0 \tag{23}$$

$$\vec{B} = \vec{B}_o + \vec{b}\,; \qquad \vec{J} = \nabla\times\vec{B}/\mu\,; \qquad \vec{F}_L = \vec{J}\times\vec{B}$$

In both above methods, the Lorentz force is applied as a source term in the momentum equations.

2.8. Effect of magnetic field on turbulence in RANS turbulence models

Many researchers [12-15, 46] improved the conventional non-MHD RANS turbulence models for the effect of the magnetic field on the turbulence in low magnetic Reynolds number liquid metal MHD flows. Ji and Gardner [14] proposed and tested source terms for magnetic field damping effects on turbulence using a k-ε model on a turbulent conducting liquid flow in an insulated pipe. Velocity profiles, skin friction, temperature profiles, Nusselt numbers showed agreement with available experimental data for range of Re and Ha. The biggest shortcoming of this model is the dependence of the turbulence damping terms on bulk flow, making the model applicable only in problems where the bulk Stuart number (or interaction parameter, $\mathrm{Ha}^2/\mathrm{Re}$) is readily defined. Smolentsev et al [15] proposed different source terms for k-ε models but again

based on bulk Stuart number. The model was found to match experiments closely in free surface channel flow.

Galperin [46] proposed a second-moment closure model for MHD turbulence, although this model was not numerically tested on conventional flows. Kenjereš and Hanjalić [12-13] proposed new source terms for k-ε and second-moment closure models (RSM). The improved k-ε model was validated with the DNS results in a channel flow under transverse magnetic field. After validation, the model was used in a 3-d developing rectangular duct flow with partial magnetic field and model was found performing well for mean velocities. No assessment for turbulence parameters was made in rectangular duct flow. Kenjereš and Hanjalić [12-13] also proposed a similar closure for $\overline{u_i u_j}$ equations for MHD effects in RSM as proposed by Galperin [46]. This closure for RSM showed considerable improvement of results in a channel flow. The current study includes the models proposed by Kenjereš and Hanjalić's [12-13] for the channel and square duct flows. The following modifications were made to the models.

2.8.1. k-ε model :

k-equation: $$S_k^M = -\sigma B_0^2 k \exp\left(-C_1^M \left(\sigma/\rho\right) B_0^2 \left(k/\varepsilon\right)\right) \tag{24}$$

ε-equation: $$S_\varepsilon^M = -\sigma B_0^2 \varepsilon \exp\left(-C_1^M \left(\sigma/\rho\right) B_0^2 \left(k/\varepsilon\right)\right) \tag{25}$$

where, $C_1^M = 0.025$

2.8.2. Reynolds Stress Model (RSM) MHD source terms:

After simplification for y-directional (vertical) magnetic field and some algebra the six independent Reynolds stress transport equations can be derived with the following MHD source terms;

$\overline{w'w'}$-equation: $S_{w'w'}^M = \sigma\left(-2B_{y0}\overline{w'\partial\phi'/\partial x} - 2B_{y0}^2\overline{w'w'}\right)$ (26)

$\overline{v'v'}$-equation: $S_{v'v'}^M = 0$ (27)

$\overline{u'u'}$-equation: $S_{u'u'}^M = \sigma\left(2B_{y0}\overline{u'\partial\phi'/\partial z} - 2B_{y0}^2\overline{u'u'}\right)$ (28)

$\overline{u'v'}$-equation: $S_{u'v'}^M = \sigma\left(B_{y0}\overline{v'\partial\phi'/\partial z} - B_{y0}^2\overline{u'v'}\right)$ (29)

$\overline{w'u'}$-equation: $S_{w'u'}^M = \sigma\left(-B_{y0}\overline{u'\partial\phi'/\partial x} + B_{y0}\overline{w'\partial\phi'/\partial z} - 2B_{y0}^2\overline{w'u'}\right)$ (30)

$\overline{w'v'}$-equation: $S_{w'v'}^M = \sigma\left(-B_{y0}\overline{v'\partial\phi'/\partial x} - B_{y0}^2\overline{w'v'}\right)$ (31)

Source term for scalar dissipation rate (ε) is defined as [13]; $S_\varepsilon^M = 0.5 S_{ii}^M \varepsilon / k$ (32)

It can be seen that all the source terms due to the magnetic field are negatively correlated with the corresponding Reynolds stress therefore sinks to the Reynolds stresses. It is interesting to note that the magnetic field causes no direct sink to the Reynolds normal stress parallel to magnetic field (i.e. $\overline{v'v'}$). The indirect suppression effect on $\overline{v'v'}$ is via Reynolds shear stresses. In the above sinks, the terms involving correlation of velocity fluctuation with electric potential gradient require modeling and cannot be incorporated directly in RSM. Kovner and Levin [47] suggested a way to model electric potential-velocity correlation. Galperin [46] and later Kenjereš and Hanjalić [12-13] followed their method and came up with following formulation for the correlation; $\partial\phi'/\partial x_k = \beta\varepsilon_{kmn} u_m' B_{n0} \Rightarrow \overline{u_i' \partial\phi'/\partial x_k} = \beta\varepsilon_{kmn} \overline{u_i' u_m'} B_{n0}$ (33)

Galperin [46] proposed $0 < \beta < 1$. Kenjereš and Hanjalić [13] proposed $\beta = 0.6$ via MHD channel flow. In the current work, the value of β as proposed by Kenjereš and Hanjalić is used.

The above discussed two formulations for k-ε and RSM for the effect of magnetic field on turbulence have been implemented using a UDF with the magnetic induction and the electric potential methods [30]. More details on various turbulence models, wall treatment approaches, magnetic induction and electric potential method for MHD calculations can be found in [30].

3. DNS Databases

Five DNS databases were used to assess the above models. The conditions for various DNS databases are given in Table 3.

3.1. High-Reynolds Number Non-MHD channel flow

Satake et al [48] performed DNS calculations in a non-MHD channel at a bulk Reynolds number of ~45818 using 800 million nodes. The mean velocities, RMS of velocity fluctuations and TKE budgets were reported. This non-MHD case was used as a base case to first evaluate the purely hydrodynamic models.

3.2. Low-Reynolds Number MHD and Non-MHD channel flows

The non-MHD channel flow data of Iwamoto et al [49] has been used to test performance of RANS models at lower Reynolds numbers. In his case, Re_τ (=$\delta u_\tau/\nu$)=150, corresponding to bulk Re (=$2\delta W_b/\nu$, δ: half channel height)=4586 was used. To test the models for MHD turbulence, the MHD channel case of Noguchi et al [50] (Re_τ (=$\delta u_\tau/\nu$)=150, bulk Re (=$2\delta W_b/\nu$)=4710, Ha (=sqrt($\sigma/\rho\nu$)$B_0\delta$)=6), δ: half channel height) was used.

3.3. Low-Reynolds Number MHD and Non-MHD square duct flows

A GPU based code (CU-FLOW) [51] that has been previously used for DNS calculations in a non-MHD square duct has been extended for DNS calculations of a MHD square duct [52]. For the non-MHD case, ($Re_\tau(=Du_\tau/\nu)=360$, bulk Re ($=DW_b/\nu$)=5466), a duct of size of 1x1x8 non-dimensional units and 160x160x1024 control volumes (with 1% grid stretching in wall normal directions) were used. For the MHD case, ($Re_\tau(=Du_\tau/\nu)=361$, bulk Re ($=DW_b/\nu$)=5602, Ha ($=sqrt(\sigma/\rho\nu)B_0D$)=21.2)) a duct of size of 1x1x16 non-dimensional units with 128x128x512 control volumes (with 2% grid stretching in wall normal directions) were used. Both these simulations were shown to give grid-independent solutions to the relevant equations.

4. COMPUTATIONAL DETAILS

4.1. Computational Domain, Boundary Conditions and Numerical Method

Taking advantage of fully-developed flow with RANS models, the domain size was taken as 1x1x1 non-dimensional units for both the channel and the square duct. For the channel, the top and the bottom walls were electrically insulated with no-slip velocity conditions while the streamwise (z-) and spanwise (x-) directions were considered periodic. In the square duct, the four walls (top, bottom, right and left) were electrically insulated with no-slip velocity conditions whereas the streamwise direction (z-) is periodic. For the MHD calculations, the magnetic field was applied in the vertical (y-) direction. The simulations were carried out by fixing the bulk mean flow Reynolds number as given in Table 3 with the mean streamwise pressure gradient free to change. All the calculations were performed using FLUENT's steady-state segregated solver with SIMPLE algorithm for pressure-velocity coupling with either magnetic induction or electric potential methods for MHD calculations [30]. For each case, the results were ensured to be grid-independent by systematically increasing the number of control volumes until a grid-independent solution is obtained. All cases were converged such that the unscaled absolute residuals reached below 10^{-3} to stagnant values.

4.2. Grids

For the high-Re calculations (case 1, Re=45818) with EWT, five grids with ten control volumes each in streamwise (z-) and spanwise (x-) directions were used. In the wall-normal (y-) direction, three uniform grids (consisting of 50, 80 and 130 control volumes) and two non-uniform grids (near-wall y+ = 1) were used. Figure 1 compares the TKE along the wall normal direction in the case of the RKE model with EWT. The results show grid independence as y^+

approached a value of one in the cells adjacent to the wall. The coarse grids produced peaks in k near the wall that appear closer to the true DNS solution. This occurs if the cell next to the wall is in the buffer region for the models with EWT. However, the trend is better-matched with the fine grids. Similar behavior was seen for the other high-Re models (RNG, SKE and RSM-LPS); hence grid independence plots for other models are not presented. All models obtained grid independence with a 139(non-uniform)x10x10 grid, so this grid was used for evaluation of these models. For the models using the SWF and NEWF approaches, the first cell center next to the wall should be placed in the range of $30 \le y^+ \le 300$ and, arbitrary grid refinement close to the wall is not appropriate. Hence, only uniform grids of 30x10x10 with y^+ in cells next to the wall being in the range of 35-40 are used for models with these wall functions.

For low-Reynolds number flows (cases 2-5), the number of cells required to satisfy near-wall $y^+>30$ is too small to be accurate. Hence, SWF and NEWF were not evaluated for low-Re flows. Only low-Re models (Abid, LB, LS, YS, AKN, and CHC) or high-Re models (like SKE, RNG (with low-Re differential viscosity model), RKE, and RSM-linear pressure-strain) with EWT are considered. Two uniform (50x10x10 and 80x10x10) and one non-uniform (100x10x10) grids were used for RKE, SKE, RNG, and RSM-LPS models with EWT to ascertain grid independency. The same grids were also used for the RSM-Sω (with low-Re correction) model. Figure 2 shows the TKE for different grids predicted by SKE with EWT. Similar behavior was seen by other models as well. As the grid is refined to 100 non-uniformly-spaced cells, the results show very good grid independence. Hence this grid is used in all subsequent computations of low-Re cases with these models. For the square duct, the same grid is used in both the wall-normal directions (i.e. 100 x 100 x 10 cells).

Grid-convergence tests were also systematically done for each of the six low-Re k-ε models. Figure 3 shows one plot of TKE in the Abid model for three different grids. All low-Re k-ε models were observed to achieve grid independence with 120 cells in the wall normal direction (giving a near-wall y^+ between 0.55-0.9). Hence this grid is used in all subsequent computations of low-Re cases with these models. In square duct flows, the same grid resolution of 120 cells is used in both wall-normal directions (i.e. 120x120x10).

4.3. Computational Costs

Due to their varying complexities and convergence rates, both the total and per-iteration computational times for each model were different. Table 4 summarizes the time per iteration

and total number of iterations to final convergence required by FLUENT (using 6 cores of a Dell Precision T7400 workstation with 2.66 GHz Intel Xeon processor and 8 GB RAM) with different models. As expected, the two equation models RKE, RNG and SKE with EWT require nearly the same time (per iteration as well as total time). On a per-iteration basis, the various two equations models are 5-30% less expensive than RSM-LPS (which solves 7 transport equations) with EWT. However, to obtain final converged results, RSM-LPS model is ~13-26 times more expensive. With SWF and NEWF, the two equation models are about 20-30% less expensive than RSM-LPS when compared on a per iteration basis but the time required to final convergence by RSM-LPS model reduces and it is only slightly more expensive. It seems that with finer grids, RSM-LPS model becomes increasingly expensive to achieve final convergence relative to two equation models. The EWT and SWF/NEWF are almost equally expensive for the same grid, but the grid required for EWT is much higher. In all models tested, the computational requirement increases almost linearly with the grid size. Surprisingly, low-Re RSM-Sω model, which also solves 7 equations, is only about twice as expensive as the two equation models. All low-Re k-ε models take nearly the same time per iteration, but the total times for LB and LS models are smaller. YS model took five times more time than LB and LS.

5. RESULTS AND DISCUSSION

Results are first presented for non-MHD flows to show the accuracy of the various models without magnetic field. From these, models giving the best agreement are evaluated for the MHD flows after incorporating the changes due to the magnetic field effects.

5.1. High-Reynolds number non-MHD channel flow (Re=45818)

Figure 4 compares the TKE predicted by the various models with the DNS data of Satake et al. [48] for the grid independent mesh with EWT. It is seen that all models (RKE, RNG, SKE, and RSM-LPS) give nearly the same distribution of the TKE. They underestimate the DNS peak values near the wall by 22-27%. Error decreases with distance from the wall, and TKE in the central core is predicted within 10%. Figure 5 shows similar behavior comparing models with SWF. As theoretically required, the near-wall y^+ has been maintained around 36-37. The results with SWF were nearly the same as with the NEWF probably because of the lack of flow separation or pressure gradient effects in a channel flow. As seen with the EWT, the peak value of TKE was again under-predicted, this time by a larger amount (42%). The agreement in the core region is much better with all the models, except RKE giving slightly lower predictions.

The non-dimensionalized mean axial velocities predicted with the SKE and RSM-LPS models using EWT and SWF are presented in Fig.6. The velocity profiles with NEWF are not presented as they were nearly the same as with SWF. It is seen that the EWT with y^+=1 resolves velocity accurately all the way up to the viscous sublayer and matches best with the DNS results across the whole channel. Both models performed equally well with EWT, with errors consistently within 3%. With SWF, as y^+ is maintained ~36, the cell next to the wall stays in log-law region. Again both models predicted mean velocities well, although error with the RSM-LPS model increased to ~5% in the central core.

The Reynolds normal stresses predicted by the RSM-LPS model with all 3 wall treatments are compared with the DNS data in Figs. 7(a) and (b). With SWF and NEWF, the predictions matched closely with the DNS data in the core region except for the wall normal velocity fluctuations, which were underpredicted. The errors increased towards the wall especially in the axial and wall normal velocity fluctuations. Both wall functions performed equally but both missed the peak values close to the wall in all the three velocity fluctuations. The peak value of the RMS of axial velocity fluctuations is underpredicted by ~36% while the error in transverse and spanwise velocity fluctuations is smaller. The RMS of spanwise velocity fluctuations matched best with the DNS. The RSM-LPS model with EWT performed better than with SWF or NEWF in predicting all three velocity fluctuations, as expected. Again, the spanwise velocity fluctuations were predicted most accurately followed by wall normal fluctuations. The error in predicting peak value of axial velocity fluctuations reduced from ~36% to ~12% by using the EWT. Overall, RSM-LPS with EWT predicted the anisotropy of Reynolds normal stresses reasonably well.

The mean streamwise pressure gradient predicted by various models is compared with the DNS data in Table 5. Overall, all models predicted the frictional losses within 10% error. The predictions with EWT were better than with SWF and NEWF.

5.2. Low-Reynolds number non-MHD channel flow (Re=4586)

We next consider the low-Re non-MHD channel flow for which the various low-Re turbulence models are first evaluated. Figure 8 compares the TKE predicted by various low-Re k-ε models with the DNS. The LS model greatly overpredicted throughout the domain, while the CHC model underpredicted near the wall and matched in the core. The 4 remaining models predicted similar values, matching the DNS data within 15% error near the wall but over-

predicting (by ~60%) in the core. Overall, the LB model performed the best of all the models. The YS model gave the correct trend across the whole domain, consistently overpredicting by 7-30%. The best low-Re k-ε models (LB, AKN, and YS) are evaluated for mean axial velocity predictions in Figure 9. All three models predicted the mean axial velocity profile across the channel very well (within 5% error).

In addition to the low-Re k-ε models, the high-Re k-ε models with EWT (RKE, RNG with differential viscosity, and SKE) and RSM models (RSM-LPS with EWT and RSM-Sω low-Re) also have been evaluated in this low-Re non-MHD channel flow. Figure 10 compares TKE predicted by these models. All models, except RNG and RSM-Sω, performed similarly by matching the peak values but over-predicting the values significantly (by ~120%) in the core. The RNG model overpredicted slightly more in the core than other models. RSM-Sω model matched TKE better in the core. Figure 11 compares the RMS of velocity fluctuations predicted by low-Re RSM-Sω and RSM-LPS model with the DNS. The RSM-Sω model, although it predicted the TKE best in the core, did not capture the anisotropy of Reynolds stresses even qualitatively. Because it was outperformed by the RSM-LPS model, the RSM-Sω model was not considered further in this study. The RSM-LPS model with EWT captured anisotropy qualitatively in all velocity fluctuations but overpredicted in the core. Figure 12 shows the comparison of the mean axial velocities given by RKE, SKE, and RSM-LPS models. All matched the DNS data closely except for some underprediction in the core.

Table 5 presents the mean streamwise pressure gradient predicted by various models for this flow. The best prediction of pressure gradient is by low-Re LB model (within 2% error) followed by the RSM-Sω model (3% error). All high Reynolds number k-ε models with EWT overpredicted the pressure gradient by ~10%. The LS and CHC models were unreasonable, with frictional loss errors of ~95% and -16%. The other low-Re models predicted friction loss within 7%.

5.3. Low-Reynolds number MHD channel flow (Re=4710, Ha=6)

The models (LB, SKE, and RSM-LPS) which performed better in low-Re non-MHD channel flow were then tested in low-Re MHD channel flow at a Reynolds number of 4710 and Ha = 6.0. Comparison of the computed TKE using the selected turbulence models with and without inclusion of the MHD sources/sinks is shown in Figure 13. The LB low-Re k-ε model with MHD sources/sinks matches the DNS computed turbulent kinetic energy quite well in the

core but underpredicts the high values close to the wall calculated by the DNS. This match in the core seems to be fortuitous when overall trend is not predicted that well by this model. The peak TKE is seen to be better predicted by LB without the MHD sources. The effect of the MHD sources/sinks on suppressing turbulence is clearly seen. SKE and RSM with EWT matched the peak values closely but overpredicted greatly (by 300-500%) in the core. The models using EWT show very little effect of MHD source terms. This is likely due to the lack of magnetic field effects in wall treatment method. This contrasts with the strong effect observed in the low-Re LB model, where the source terms are applied throughout the domain.

Figure 14 compares the axial velocity in wall coordinates. The LB low-Re k-ε model with MHD sources gives the best agreement with DNS data. However, part of profile in between $15<y^+<80$ is under-predicted. The second best prediction is from the LB model without MHD sources. The predictions of RSM and SKE are similar, with the RSM-LPS performing slightly better. The underprediction of the normalized velocity in the core is mainly due to the higher frictional losses leading to higher friction velocity. The SKE and RSM models with EWT do not show much effect of MHD sources in the mean velocity. Figure 15 compares the axial velocity, as in Figure 14, but this time non-normalized mean velocity as a function of distance from the wall in the wall normal direction. The close match of predictions from all models with the DNS reinforces the assertion that the higher frictional losses are causing the differences in predictions in Figure 14.

We next examine the MHD source/sink terms in the k-equation and compare their magnitude with those extracted from the DNS budgets (Fig. 16). The trends predicted by all 3 models are reasonable, but the LB low-Re k-ε model matches best with the DNS (within 20%). Although, the SKE model predicts the peak closely, it overpredicts the values in the core by ~300%. Interestingly, none of the models capture the small positive peak very close to the wall.

Figure 17 presents the sink term due to magnetic field in the turbulent dissipation rate (ε) equation. All 3 models correctly predict the asymptotic decay of source to dissipation to zero in the core. The LB low-Re model correctly predicts the profile qualitatively across the whole channel but underestimates the values. The SKE and RSM models predict qualitatively similar profiles with negative peaks at $y^+\sim10$. The SKE model gives the closest match although errors approach 50% near the wall.

Figures 18 and 19 give comparisons of the magnetic field source/sink terms in Reynolds normal stresses obtained by RSM-LPS. For S^{M+}_{ww}, RSM behaves similar to the TKE source. It underpredicts the peak value and overpredicts in the core. The positive values, which indicate a source in S^{M+}_{ww} below $y^+<5$, are again missed by the model. The MHD sink in S^{M+}_{uu} is qualitatively captured but the values are over-predicted across the whole length.

For this case, the LB model with MHD sources predicts the pressure gradient closest to the DNS (within 2.5%) followed by LB without MHD sources (Table 5). The SKE and RSM models overpredict the pressure gradient by about 20%. Adding the MHD sources improves the predictions only slightly.

5.4. Low-Reynolds number non-MHD square duct flow (Re=5466)

The models are next evaluated for the fully-developed turbulent flow in a square duct bounded by four walls. For this case, it is well-known that the anisotropy in the Reynolds stresses generates cross-stream flows [16], which are not present in the laminar case. Turbulence models based on isotropic eddy-viscosity cannot predict such secondary flows [16]. To predict the secondary flows, it is necessary to use either non-linear/anisotropic two equation models [53-56], RSMs [57], or algebraic stress models [58-59]. Hence, models other than the above are not expected to be accurate. However, they have been considered in this study to assess their inaccuracy and to evaluate their relative performance against the more expensive RSM. Figure 20 presents the comparison of TKE along vertical bisector in a non-MHD square duct using LB, RKE, SKE and RSM-LPS models. The grid in all models resolved the flow up to the viscous sublayer ($y^+\sim1$). The LB model predicts the TKE better than other models. However, all models give excessive TKE in the core region by over 100%. Figure 21 compares the predicted RMS of velocity fluctuations by the RSM model along vertical bisector of the duct. RSM-LPS model with EWT, even when used with near wall spacing of $y^+<1.1$, over-predicts all the components of Reynolds normal stresses in the core by 40-75%. The agreement is however better in the near-wall region.

Figure 22 compares the mean axial velocity along the vertical bisector obtained by the different models. The RKE, SKE and LB models show similar reasonable behavior, as they agree with the DNS within ~8%. All 3 models overpredict in-between the wall and the core and underpredict in the core region. The RSM model expectedly is slightly better but matches the other models in underpredicting the core region. Compared to the channel, the square duct flow

is predicted with less accuracy, probably as a result of the inability to predict the secondary flows. Figure 23(a) and (b) compare the mean axial velocity contours and secondary velocity vectors of the RSM-LPS model with the DNS. Bulging of axial velocity is underpredicted. The other models cannot predict secondary flows so are not shown.

Table 5 compares the mean streamwise pressure gradient predictions with the DNS. The LB model is best with an error of only ~7%. The RSM overpredicts pressure gradient by ~25% which is worst. SKE and RKE overpredict by ~12.0%.

5.5. Low-Reynolds number MHD square duct flow (Re=5602, Ha=21.2)

The final test case is MHD square duct flow, which is an appropriate geometry for the industrial application of electromagnetic, such as control of nozzle flow in the continuous casting of steel. The magnetic field causes different flow profiles along the vertical and the horizontal bisectors in the square duct. Both the magnetic induction and electric potential methods in FLUENT were tested. Both methods gave virtually identical result, which was expected because the maximum induced magnetic field is only 0.039% of the externally applied field.

Figures 24 and 25 compare TKE along vertical and horizontal bisectors respectively. The DNS shows that MHD suppresses turbulence more along the vertical bisector. Only the LB model with MHD sources predicts this trend, matching with DNS generally within 50%. Without MHD sources, the LB model overpredicts DNS by 100-500%. The MHD sources/sinks [12-13] provide significant improvement by predicting the correct trend of turbulence suppression, especially using the LB model. Both the RKE and RSM models over-predict the turbulence energy in the core along both the bisectors by ~500%. Moreover they do not capture the strong differential suppression of turbulence along the two bisectors, as was seen in the DNS and in the results of LB model with MHD sources. On the horizontal bisector close to the side walls, turbulence is not suppressed much because the induced current is parallel to the magnetic field in this region. The RKE and RSM models predict the peak TKE better along the horizontal bisector. Surprisingly, the RSM model is found to perform the worst among the tested models for suppressing turbulence by magnetic field effects.

Figure 26 and 27 give the mean axial velocity predictions from various models compared with the DNS along vertical and horizontal bisectors respectively. The DNS solution shows less flattening along the vertical bisector, which shows the importance of the secondary flows and the anisotropic suppression of turbulence by the magnetic field. All tested models predict about the

same velocity profile along both bisectors. They match the DNS within ~4% along the horizontal bisector and overpredict velocity flattening along the vertical bisector by ~30%. The LB and RSM-LPS models are no better than the other models. MHD sources produce higher velocities, due to suppressing turbulence somewhat, but the agreement with DNS is not improved.

Figure 28 presents mean axial velocity contours and mean secondary velocity vectors in the cross-section. As shown by the DNS, the mean axial velocity contours and the secondary flows are significantly altered in the presence of the transverse magnetic field. The secondary velocities, rather going into corners, now go towards the top and bottom walls, thus lifting the axial velocity contours in these regions towards the top and the bottom walls. After hitting the walls, these secondary flows move parallel to the top and bottom walls before turning towards the core at the center and thus cause a strong bulging in mean axial velocity there. This effect of strong bulging is not seen close to the side walls. It can be seen that none of the models is able to capture this effect. Although RSM predicts secondary flows, the differential effect of the magnetic field close to the top /bottom walls and the right/left side walls is missing. RSM predicts almost symmetric mean secondary and axial velocities except for a slight elongation of mean axial velocity (i.e. flattening) in the vertical direction. As mentioned earlier, LB and RKE do not predict secondary flows at all and over-predict the velocity flattening in the vertical direction, as also seen in the line plots of Fig. 26. Both the k-ε models (LB and RKE) predict similar axial velocity across the cross-section.

Figure 29 and 30 show the MHD sources/sinks in the TKE equation computed by the various models. The velocity-electric potential gradient correlation acts as a source whereas the Reynolds normal stresses perpendicular to the magnetic field act as sinks, as shown in the DNS data. The sink is stronger than the source giving a net effect of suppressing the turbulence. It can be seen that the LB model predicts this source reasonably correctly, followed by RKE and then RSM-LPS. The predictions are better along the stronger Lorentz force bisector. Both the RKE and the RSM-LPS over-predict the MHD sources to TKE along both bisectors.

The friction factor along bottom horizontal and left vertical walls is presented in Fig. 31. Along the bottom horizontal wall, the friction factor shows two side peaks with a large dip at the center. Along left-vertical wall, the friction factor shows a central flat region with two side dips. None of the models is seen to predict these trends correctly. Both the k-ε models (LB and RKE)

give similar profiles, with a central overpredicted peak. The RSM-LPS model predicts the side peaks with a central dip along both walls but does not completely agree with the DNS results. RSM suggests larger frictional losses, especially in the corners. The best agreement is seen with LB model with MHD sources. The LB model, without MHD sources, overpredicts friction along both walls.

Finally, a comparison of mean streamwise pressure gradients computed by the various models again shows (Table 5) that the LB low-Re model with MHD sources performs best by matching within ~2% error with the DNS predictions. LB model without MHD sources is next, followed by RKE with EWT. The performance of these models is similar in the non-MHD and the MHD cases.

6. CONCLUSIONS

In this study several turbulence models of k-ε and Reynolds stress transport category are evaluated for their ability to predict turbulent flow fields subjected to a magnetic field. Five test cases of flows in a channel and square duct have been computed and the results are compared with DNS data. The MHD sources/sinks in k- and ε- equations for k-ε models and in Reynolds stresses for RSM, as proposed by Kenjereš and Hanjalić [12-13], were implemented through UDFs in the FLUENT code. The performance of these models, on the basis of their predictions of mean velocities, RMS of velocity fluctuations, TKE, MHD sources and frictional losses can be summarized as follows:

In both high- and low-Re channel flows, all of the models predicted mean axial velocity reasonably well (within 5% error), given fine-enough grids for grid-independence (EWT and low-Re) or satisfaction of the y+ requirements (SWF and NEWF). However, the TKE was much less accurate, often exceeding 60% overprediction in the core. In high-Re channel flows, models underpredicted near-wall peak turbulence energy whereas in low-Re channel flows, they showed better agreement near the wall but over-predicted values in the core. For the MHD flows, the implementation of the MHD sources improved predictions for low-Re k-ε models. The high-Re models which use the wall treatments did not show much improvement with MHD sources, perhaps due to the lack of MHD effects in the wall formulations.

In the case of low-Re square duct flows, the models tested did not predict the mean axial velocities to a good accuracy (error ranging ~8-30%) because of the secondary flows generated due to turbulence anisotropy. The TKE was overpredicted in the core, often exceeding ~60%, by

all models except LB in MHD duct. The effect of turbulence suppression by magnetic field was not properly captured on mean velocity, Reynolds stresses/turbulent kinetic energy and frictional losses by any single model in a MHD duct, even after inclusion of the MHD sources of turbulence.

For problems involving high-Re, the SKE model offers reasonable accuracy at low computational cost. Adding EWT improves accuracy slightly over standard wall laws, but significantly increases cost. For flows with low-Re number, the Lam-Bremhorst (LB) low-Re k-ε model performed better than the others in both hydrodynamic and magnetic field influenced turbulent flows. Given the need to compute complex industrial flows with efficient computational use, using these 2 models with appropriate changes for magnetic field effects provides a reasonable compromise of accuracy and speed. Finally, the RSM-LPS model with EWT offers similar accuracy with the added ability of capturing turbulence anisotropy and secondary flows, but its computational cost is very high.

ACKNOWLEDGMENTS

The authors gratefully thank the Continuous Casting Consortium, Department of Mechanical Science & Engineering, University of Illinois at Urbana-Champaign, IL, and the National Science Foundation (Grant CMMI-07-27620) for providing support for this work. We would like to thank Aaron Shinn for providing the DNS data in non-MHD square duct flow. The FLUENT code was provided by ANSYS, Inc.

REFERENCES

(1) C. G. Speziale, Analytical methods for the development of Reynolds-stress closures in turbulence, Annu. Rev. Fluid Mech., 1991, Vol. 23, pp. 107–57.

(2) C. M. Hrenya, E. J. Bolio, D. Chakrabarti, and J. L. Sinclair, Comparison of low Reynolds number k-ε turbulence models in predicting fully developed pipe flow, Chemical Engineering Science, 1995, Vol. 50, No. 12, pp. 1923-1941.

(3) R. Martinuzzi and A. Pollard, Comparative study of turbulence models in predicting turbulent pipe flow Part I: Algebraic stress and k-ε models, AIAA Journal, 1989, Vol. 27, No. 1, pp. 29-36.

(4) A. Pollard, and R. Martinuzzi, Comparative study of turbulence models in predicting turbulent pipe flow Part II: Reynolds stress and k-ε models, AIAA Journal, 1989, Vol. 27, No. 12, pp. 1714-1721.

(5) S. Thangam, and C. G. Speziale, Turbulent separated flow past a backward-facing step: A critical evaluation of two-equation turbulence models, NASA contractor Report 187532, 1991, ICASE Report No. 91023.

(6) C. J. Steffen, Critical comparison of several low Reynolds number k-ε turbulence models for flow over backward facing step, AIAA, 1993, 93-1927, 29th AIAA, SAE, ASME and ASEE, Joint Propulsion Conference and Exhibit.

(7) J.-Y. Kim, A. J. Ghajar, C. Tang, and G. L. Foutch, Comparison of near-wall treatment methods for high Reynolds number backward-facing step flow, Int. J. of Computational Fluid Dynamics, 2005, Vol. 19, No. 7, pp. 493-500.

(8) S. H. Seyedein, M. Hasan, A. S. Majumdar, Modeling of a single confined slot jot impingement using various k-ε turbulence models, Appl. Math. Modeling, 1994, Vol. 18, pp. 526-537.

(9) E. W. Miner, T. F. Swean Jr., R. A. Handler, and R. I. Leighton, Examination of wall damping for the k-ε turbulence model using direct simulation of turbulent channel flow, Int. J. for Numerical Methods in Fluids, 1991, Vol. 12, pp. 609-624.

(10) T. Kobayashi, and S. Togashi, Comparison of turbulence models applied to backward-facing step flow, JSME International Journal, 1996, Series B, Vol. 39, No. 3, pp. 453-460.

(11) X.-D. Yang, H.-Y. Ma, Y.-N. Huang, Prediction of homogeneous shear flow and a backward-facing step flow with some linear and non-linear k-ε turbulence models, Communications in Nonlinear Science and Numerical Simulation, 2005, Vol. 10, pp. 315-328.

(12) S. Kenjereš, K. Hanjalić, On the implementation of effects of Lorentz force in turbulence closure models. Int. J. Heat Fluid Flow, 2000, Vol. 21, pp. 329-337.

(13) S. Kenjereš, K. Hanjalić and D. Bal, A direct-numerical-simulation-based second-moment closure for turbulent magnetohydrodynamic flows, Phys. Fluids, 2004, Vol. 16, No. 5, pp. 1229-1241.

(14) H-C Ji, R. A. Gardner, Numerical analysis of turbulent pipe flow in a transverse magnetic field. Int. J. Heat Mass Transf., 1997, Vol. 40, pp. 1839-1851.

(15) S. Smolentsev, M. Abdou, N. Morley, A. Ying, T. Kunugi, Application of the "k-ε" model to open channel flows in a magnetic field, Int. J. Eng. Sci., 2002, Vol. 40, pp. 693-711

(16) T. Kajishima, and Y. Miyake, A discussion on eddy viscosity models on the basis of the large eddy simulation of turbulent flow in a square duct, Computers & Fluids, 1991, Vol. 21, No. 2, pp. 151-161.

(17) B. E. Launder and D. B. Spalding, Lectures in mathematical models of turbulence, Academic Press, 1972, London, England.

(18) V. Yakhot and S. A. Orszag, Renormalization group analysis of turbulence: I. Basic theory, Journal of Scientific Computing, 1986, Vol. 1, No. 1, pp. 1-51.

(19)T.-H. Shih, W. W. Liou, A. Shabbir, Z. Yang, and J. Zhu, A new k-ε eddy-viscosity model for high Reynolds number turbulent flows - Model development and validation, Computers & Fluids, 1995, Vol. 24, No. 3, pp. 227-238.

(20) R. Abid, Evaluation of two-equation turbulence models for predicting transitional flows, Int. J. of Engineering Science, 1993, Vol. 31, No. 6, pp. 831-840.

(21) C. K. G. Lam, and K. Bremhost, A modified form of the k-ε model for prediction of wall turbulence, Transactions of ASME, Journal of Fluids Engineering, 1981, Vol. 103, pp. 456-460.

(22) B. E. Launder, and B. I. Sharma, Application of the energy-dissipation model of turbulence to the calculation of flow near a spinning disc, Lett. Heat Mass Transf., 1974, Vol. 1, pp. 131-138.

(23) Z. Y. Yang and T.-H. Shih, A new time scale based k-ε model for near-wall turbulence, AIAA Journal, 1993, Vol. 31, No. 7, pp. 1191-1198.

(24) K. Abe, T. Kondoh, and Y. Nagano, A new turbulence model for predicting fluid flow and heat transfer in separating and reattaching flows I: Flow field calculations, Int. J. Heat Mass Transfer, 1994, Vol. 37, No. 1, pp. 139-151.

(25) K. C. Chang, W. D. Hsieh and C. S. Chen, A modified low-Reynolds-number turbulence model applicable to recirculating flow in pipe expansion, Transaction of the ASME, Journal of Fluids Engineering, 1995, Vol. 117, pp. 417-423.

(26) W. D. Hsieh and K. C. Chang, Calculation of wall heat transfer in pipe-expansion turbulence flows, Int. J. Heat Mass Transfer, 1996, Vol. 39, No. 18, pp. 3813-3822.

(27) M. M. Gibson and B. E. Launder. Ground effects on pressure fluctuations in the atmospheric boundary layer. J Fluid Mech., 1978, Vol. 86, pp. 491-511.

(28) B. E. Launder, Second-moment closure: Present... and Future? Inter. J. Heat Fluid Flow, 1989, Vol. 10, No. 4, pp. 282-300.

(29) B. E. Launder, G. J. Reece, and W. Rodi, Progress in the development of a Reynolds-stress turbulence closure, J. Fluid Mech., 1975, Vol. 68, No. 3, pp. 537-566.
(30) FLUENT6.3-Manual (2007), ANSYS Inc., 10 Cavendish Court, Lebanon, NH, USA.
(31) D. C. Wilcox, Turbulence modeling for CFD, 1998, second edition, DCW Industries, Inc., California.
(32) B. E. Launder, and D. B. Spalding, The numerical computation of turbulent flows, Comput. Methods Appl. Mech. Eng., 1974, Vol. 3, pp. 269-289.
(33) S.-E. Kim and D. Choudhary, A near-wall treatment using wall functions sensitized to pressure gradient, In ASME FED Vol. 217, Separated and Complex Flows, ASME, 1995.
(34) B. Kader, Temperature and concentration profiles in fully turbulent boundary layers, Int. J. Heat Mass Transfer, 1981, Vol. 24, No. 9, pp. 1541-1544.
(35) M. Wolfstein, The velocity and temperature distribution of one-dimensional flow with turbulence augmentation and pressure gradient, Int. J. Heat Mass transfer, 1969, Vol. 12, pp. 301-318.
(36) S. B. Pope, Turbulent Flows, 2000, Cambridge University Press, Cambridge, United Kindom.
(37) H. K. Versteeg, and W. Malalasekra, An Introduction to Computational Fluid Dynamics: The Finite Volume Method Approach. 1995, Essex, England: Longman Scientific Technical.
(38) F. S. Lien and M. A. Leschziner, Assessment of turbulent transport models including non-linear RNG eddy-viscosity formulation and second-moment closure, Computers & Fluids, 1994, Vol. 23, No. 8, pp. 983-1004.
(39) S. Fu, B. E. Launder, and M. A. Leschziner, Modeling strongly swirling recirculating jet flow with Reynolds-stress transport closures, 6th Symposium on Turbulent Shear Flows, 1987, Toulouse, France.
(40) B. E. Launder, Second-moment closure and its use in modeling turbulent industrial flows, Int. J. for Num. Meth. Fluids, 1989, Vol. 9, pp. 963-985.
(41) B. E. Launder and N. Shima, Second-moment closure for near-wall sublayer: development and application, AIAA Journal, 1989, Vol. 27, No. 10, pp. 1319-1325.
(42) V. C. Patel, W. Rodi, G. Scheuerer, Turbulence models for near-wall and low-Reynolds number flows: a review, AIAA, 1985, Vol. 23, No. 9, pp. 1308-1319.

(43) F. White and G. Christoph, A simple new analysis of compressible turbulent skin friction under arbitrary conditions, Technical Report AFFDL-TR-70-133, Feb. 1971.

(44) P. Huang, P. Bradshaw, and T. Coakley, Skin friction and velocity profile family for compressible turbulent boundary layers, AIAA Journal, 1993, Vol. 31, No. 9, pp. 1600-1604.

(45) R. Moreau. Magnetohydrodynamics. Kluwer Academic Publishers, 1990.

(46) B. Galperin, A second momentum closure model for MHD turbulence, J. Applied Mathematics and Physics, 1989, Vol. 40, pp. 740-757.

(47) D. S. Kovner, and V. B. Levin, Turbulent electrically conducting pipe flow in a longitudinal magnetic field, Teplofiz, Vys. Temp., 1964, 2, 742.

(48) S.-I. Satake, T. Kunugi, K. Takase, and Y. Ose, Direct numerical simulation of turbulent channel flow under a uniform magnetic field for large-scale structures at high Reynolds number, Phys. Fluids, 2006, Vol. 18, 125106.

(49) K. Iwamoto, Y. Suzuki, and N. Kasagi, Reynolds number effects on wall turbulence: Toward effective feedback control, Int. J. Heat and Fluid flow, 2002, Vol. 23, pp. 678-689.
http://www.thtlab.t.u-tokyo.ac.jp/

(50) H. Noguchi, and N. Kasagi, Direct numerical simulation of liquid metal MHD turbulent channel flows, Preprint of JSME, 1994, No. 940-53, pp. 365-366.
http://www.thtlab.t.u-tokyo.ac.jp/

(51) A. F. Shinn, S. P. Vanka, and W. W. Hwu., Direct Numerical Simulation of Turbulent Flow in a Square Duct Using a Graphics Processing Unit (GPU), AIAA-2010-5029, 40th AIAA Fluid Dynamics Conference, June 2010.

(52) R. Chaudhary, S. P. Vanka, and B. G. Thomas, Direct Numerical Simulation of Magnetic Field Effects on Turbulent Flow in a Square Duct, Phys. Fluids, Vol. 22, Issue 6, to appear June 2010.

(53) S. Nisizima, A numerical study of turbulent square-duct flow using an anisotropic k-ε model, Theoretical and Computational Fluid Dynamics, 1990, Vol. 2, No. 1, pp. 61-71.

(54) H. K. Myong, and T. Kobayashi, Prediction of three-dimensional developing turbulent flow in a square duct with an anisotropic low-Reynolds-number k-ε model, Transactions of ASME, J. Fluids Engineering, 1991, Vol. 113, pp. 608-615.

(55) C. G. Speziale, On nonlinear k-l and k-ε models of turbulence, J. Fluid mech., 1987, Vol. 178, pp. 459-475.

(56) G. Mompean, S. Gavrilakis, L. Machiels, and M. O. Deville, On predicting the turbulence-induced secondary flows using non-linear k-ε models, Phys. Fluids, 1996, Vol. 8, No. 7, pp. 1856-1868.
(57) D. Naot, A. Savit, and M. Wolfshtin, Numerical calculation of Reynolds stresses in a square duct with secondary flow, Heat and Mass Transfer, 1974, Vol. 7, No. 3, pp. 151-161.
(57) A. O. Demuren and W. Rodi, Calculation of turbulence-driven secondary motion in non-circular ducts, J. Fluid Mech. 1984, Vol. 140, pp. 189-222.
(58) W. Rodi, A new algebraic relation for calculating the Reynolds stresses, Z. Angew. Math. Mech. 1976, 56, 219.

Table 1 Damping functions and wall boundary conditions for different low-Re k-ε models*

Model	f_1	f_2	f_μ	ε_w (wall BC)
Abid	1.0	$\left(1-\frac{2}{9}\exp(-\mathrm{Re}_T^2)/36\right)^2$ $\left(1-\exp\left(-\mathrm{Re}_y/12\right)\right)$	$\tanh\left(0.008\,\mathrm{Re}_y\right)\left(1+4\,\mathrm{Re}_T^{-3/4}\right)$	$\varepsilon_w=\nu\frac{\partial^2 k}{\partial y^2}$
LB	$1+\left(0.05/f_\mu\right)^3$	$\left(1-\exp(-\mathrm{Re}_T^2)\right)$	$\left(1-\exp(-0.0165\mathrm{Re}_y)\right)^2\left(1+20.5/\mathrm{Re}_T\right)$	$\frac{\partial\varepsilon}{\partial y}=0$
LS	1.0	$\left(1-0.3\exp(-\mathrm{Re}_T^2)\right)$	$\exp(-3.4/\left(1+\mathrm{Re}_T/50\right)^2)$	$\varepsilon_w=0$
YS	$\frac{\sqrt{\mathrm{Re}_T}}{1+\sqrt{\mathrm{Re}_T}}$	$\frac{\sqrt{\mathrm{Re}_T}}{1+\sqrt{\mathrm{Re}_T}}$	$\left(1+1/\sqrt{\mathrm{Re}_T}\right)$ $\left(1-\exp\left(\begin{matrix}-1.5x10^{-04}\,\mathrm{Re}_y\\-5x10^{-07}\,\mathrm{Re}_y^3-10^{-10}\,\mathrm{Re}_y^5\end{matrix}\right)\right)^{1/2}$	$\varepsilon_w=2\nu\left(\frac{\partial\sqrt{k}}{\partial y}\right)^2$
AKN	1.0	$\left(1-0.3\exp(-\left(\mathrm{Re}_T/6.5\right)^2)\right)$ $\left(1-\exp\left(-\mathrm{Re}_\varepsilon/3.1\right)\right)^2$	$\left(1+5.0/\mathrm{Re}_T^{3/4}\exp(-\left(\mathrm{Re}_T/200\right)^2)\right)$ $\left(1-\exp\left(-\mathrm{Re}_\varepsilon/14\right)\right)^2$	$\varepsilon_w=\nu\frac{\partial^2 k}{\partial y^2}$
CHC	1.0	$\left(1-0.01\exp(-\mathrm{Re}_T^2)\right)$ $\left(1-\exp\left(-0.0631\mathrm{Re}_y\right)\right)$	$\left(1-\exp\left(-0.0215\mathrm{Re}_y\right)\right)^2$ $\left(1+31.66/\mathrm{Re}_T^{5/4}\right)$	$\varepsilon_w=\nu\frac{\partial^2 k}{\partial y^2}$

* wall BC, $k_w=0$, and $\mathrm{Re}_T=\frac{\rho k^2}{\mu\varepsilon}$, $\mathrm{Re}_y=\frac{\rho\sqrt{k}\,y}{\mu}$ and $\mathrm{Re}_\varepsilon=\frac{\rho\left(\mu\varepsilon/\rho\right)^{1/4}y}{\mu}$

Table 2 Various terms and constant of low-Re k-e models

Model	D	E	C_1	C_2	σ_k	σ_ε	C_μ
Abid	0	0	1.45	1.83	1.0	1.4	0.09
LB	0	0	1.44	1.92	1.0	1.3	0.09
LS	$2\nu\left(\frac{\partial\sqrt{k}}{\partial y}\right)^2$	$2\nu\nu_t\left(\frac{\partial^2\bar{u}}{\partial y^2}\right)^2$	1.44	1.92	1.0	1.3	0.09
YS	0	$\nu\nu_t\left(\frac{\partial^2\bar{u}}{\partial y^2}\right)^2$	1.44	1.92	1.0	1.3	0.09
AKN	0	0	1.5	1.9	1.4	1.4	0.09
CHC	0	0	1.44	1.92	1.0	1.3	0.09

Table 3 Various parameters in different DNS calculations considered during evaluation [48-52]

Geometry	Re	Grid (N_xxN_yxN_z)	Comput. Domain (XxYxZ)	Spatial resolution (Δx^+, Δy^+, Δz^+)	Ha	$W_b / d\bar{p}/dz$
Channel (Case-1)	45818 (Re_τ=1120) (Satake et al)	1024x1024x768	πx1x2.5π	9.16, 0.163-4.25, 17.2	0	20.45 / 2.0
Channel (Case-2)	4586 (Re_τ=150) (Iwamoto et al)	128x97x128	πx1x2.5π	7.36, 0.08-4.91, 18.4	0	15.28 / 2.0
Channel (Case-3)	4710 (Re_τ=150) (Noguchi et al)	64x128x64	0.5πx1x1.25π	7.36, 0.08-4.9, 9.2	6.0	15.7 / 2.0
Square duct (Case-4)	5466 (Re_τ=360) (Shinn et al)	160x160x1024	1x1x8	1.47-3.24, 1.47-3.24, 2.81 (1% stretching in x- and y-)	0	15.187 / 4.0
Square duct (Case-5)	5602 (Re_τ=361) (Chaudhary et al)	128x128x512	1x1x16	1.41-4.92, 1.41-4.92, 11.28 (2% stretching in x- and y-)	21.2	1.057/0.01857

Where, $\mathrm{Re}_\tau = \frac{D_1 u_\tau}{\nu}$, $\mathrm{Re} = \frac{D_2 W_b}{\nu}$, and $Ha = B_y D_1 \sqrt{\frac{\sigma}{\rho\nu}}$.

Channel: $D_1 = \delta$, $D_2 = 2\delta$ ($\delta = 0.5$ is half channel height)

Square duct: $D_1 = D_2 = D$, ($D = 1$ is the side of the square duct)

Table 4 **Time taken per iteration (sec) / # of iterations in final convergence** by FLUENT with various models, wall treatment methods and Reynolds numbers in non-MHD channel flow for final grids

Turbulence Model	Wall treatment method	Re=4586	Re=4586	Re=45818	
		120x10x10	100x10x10	139x10x10	30x10x10
RKE	En wall treatment	-	0.19 / 2289	0.22 / 3818	-
	Non-eq wall fn	-	-	-	0.11 / 1227
	Std wall fn	-	-	-	0.11 / 1227
SKE	En wall treatment	-	0.19/ 2289	0.23 / 3195	-
	Non-eq wall fn	-	-	-	0.11 / 954
	Std wall fn	-	-	-	0.11 / 954
RNG	En wall treatment	-	0.20 / 2700	0.24 / 3125	-
	Non-eq wall fn	-	-	-	0.11 / 954
	Std wall fn	-	-	-	0.11 / 954
RSM-LPS	En wall treatment	-	0.21 / 55033	0.29 / 38689	-
	Non-eq wall fn	-	-	-	0.14 / 2464
	Std wall fn	-	-	-	0.13 / 3115
RSM-Sω	Low-Re RSM model	-	0.22 / 4568	-	-
Abid	Low-Re k-ε model	0.20 / 5400	-	-	-
LB	Low-Re k-ε model	0.20 / 3150	-	-	-
LS	Low-Re k-ε model	0.20 / 3075	-		
YS	Low-Re k-ε model	0.20 / 17700	-	-	-
AKN	Low-Re k-ε model	0.21 / 4571	-	-	-
CHC	Low-Re k-ε model	0.21 / 5214	-	-	-

Table 5 Mean streamwise pressure gradient in different flows predicted by various models

	Channel (Re=45818)	Channel (Re=4586)	Channel (Re=4710, Ha=6) Mag-Ind Method		Square duct (Re=5466)	Square duct (Re=5602, Ha=21.2) Mag-Ind/Elec Pot Methods	
			With MHD sources	Without MHD sources		With MHD sources	Without MHD sources
DNS	2.0	2.0	2.0		4.0	0.01857	
RKE-EWT	1.97	2.20	-	-	4.46	0.0228/0.0228	-
SKE-EWT	2.02	2.20	2.40	2.47	4.46	-	-
RNG-EWT	1.99	2.20	-	-	-	-	-
RSM-LPS-EWT	2.08	2.16	2.37	2.42	5.0	0.0244	-
RKE-NWF	1.83	-	-	-	-	-	-
SKE-NWF	1.90	-	-	-	-	-	-
RNG-NEWF	1.83	-	-	-	-	-	-
RSM-LPS-NEWF	1.84	-	-	-	-	-	-
RKE-SWF	1.85	-	-	-	-	-	-
SKE-SWF	1.94	-	-	-	-	-	-
RNG-SWF	1.89	-	-	-	-	-	-
RSM-LPS-SWF	1.85	-	-	-	-	-	-
RSM-Sω	-	1.94	-	-	-	-	-
Abid	-	2.07	-	-	-	-	-
LB	-	1.97	2.04	2.18	4.28	0.0190	0.0215
LS	-	3.87	-	-	-	-	-
YS	-	2.13	-	-	-	-	-
AKN	-	2.11	-	-	-	-	-
CHC	-	1.68	-	-	-	-	-

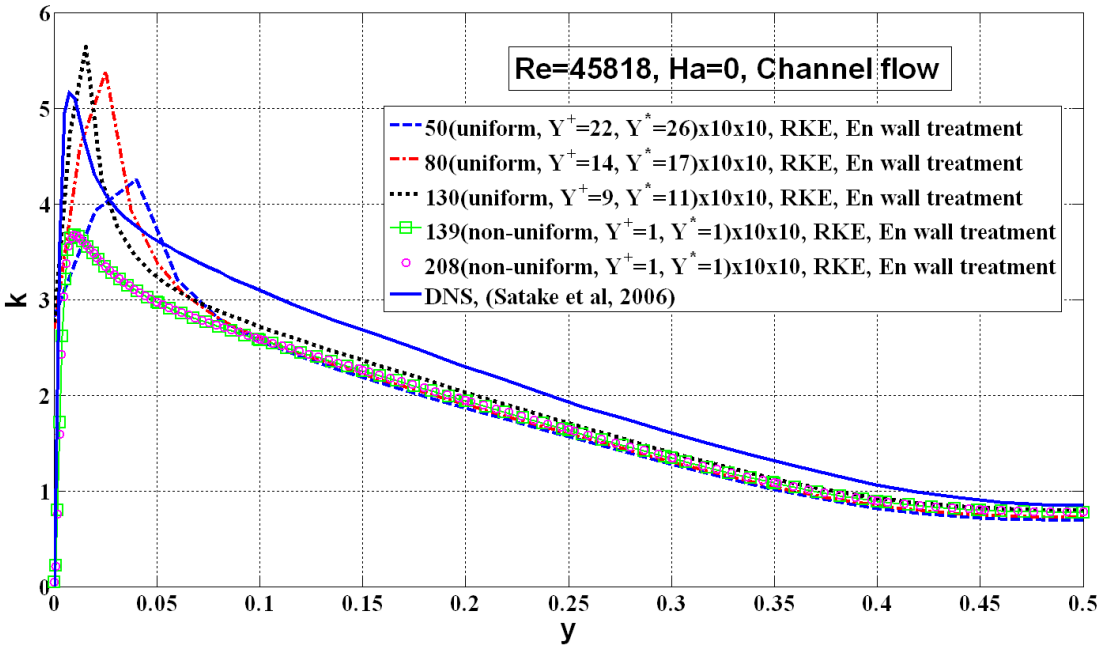

Fig-1 Grid independence study in high-Re channel flow for RKE with EWT

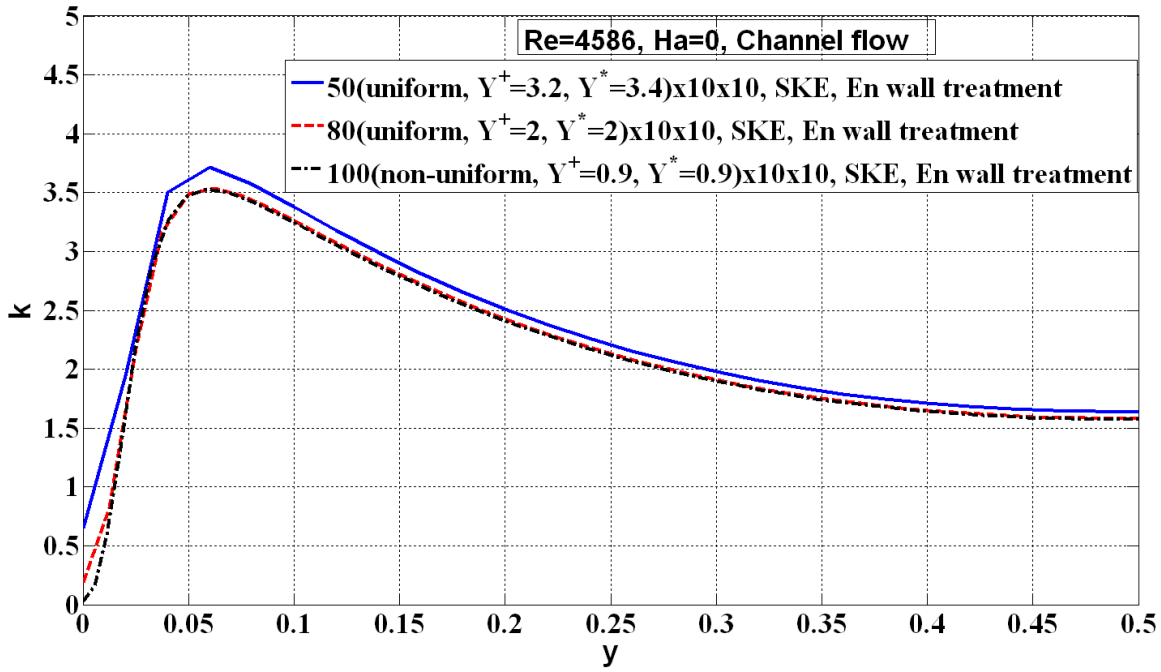

Fig-2 Grid independence study in low-Re channel flow for SKE with EWT

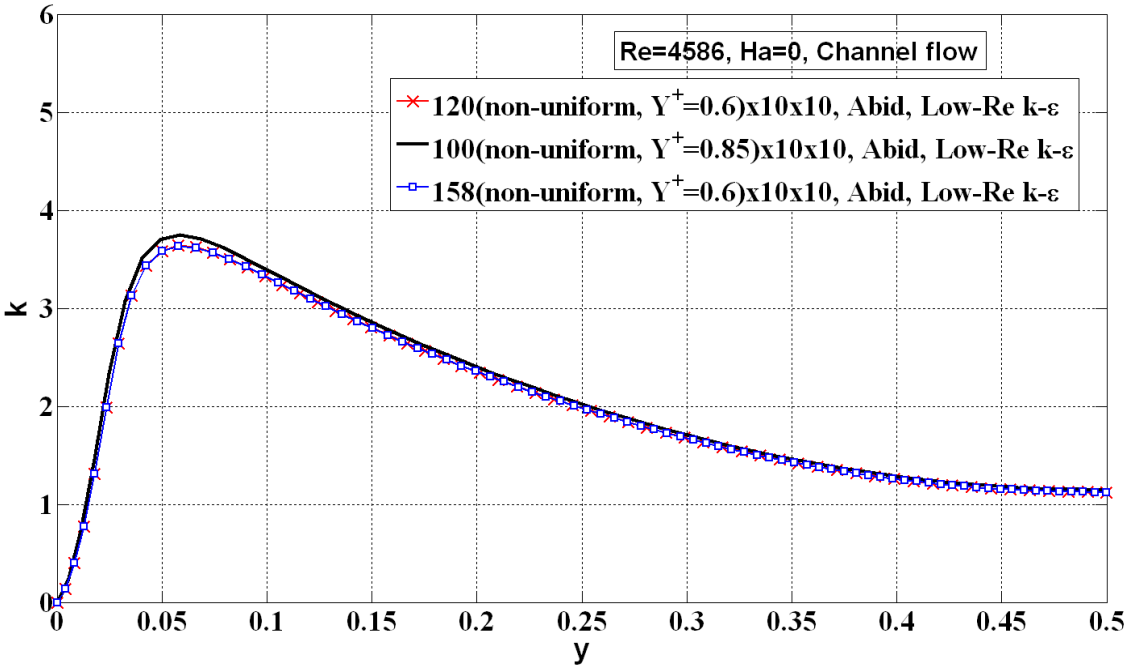

Fig-3 Grid independence study in low-Re channel flow for Abid low-Re k-ε model

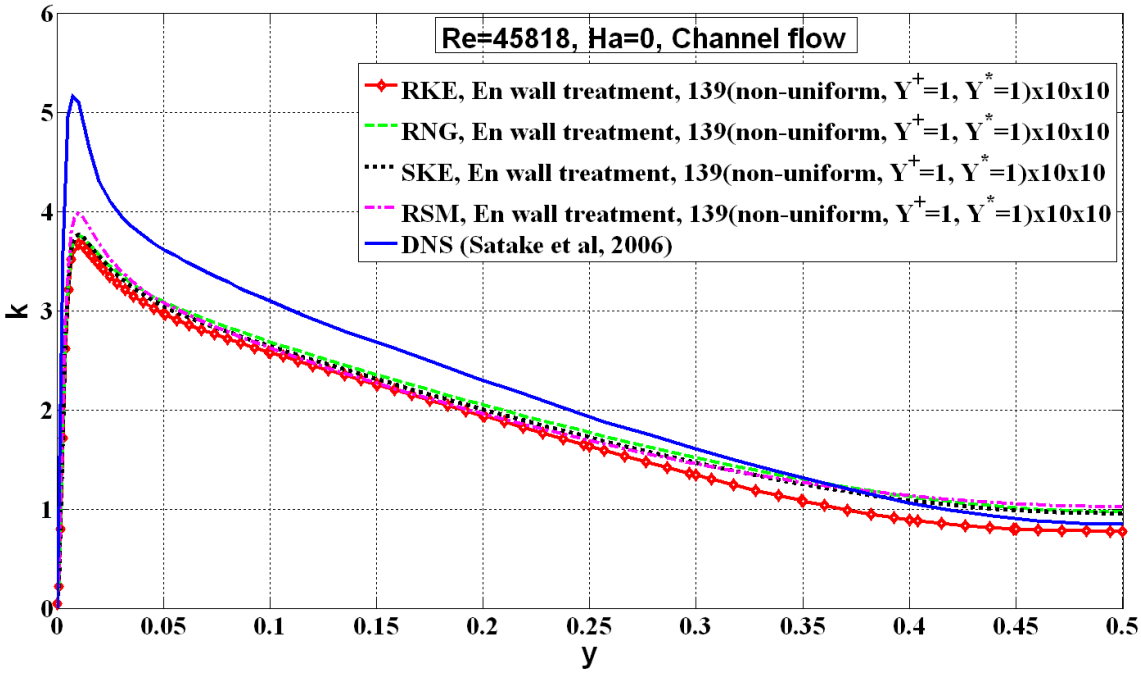

Fig-4 Comparison of TKE in various models with EWT in high-Re channel flow

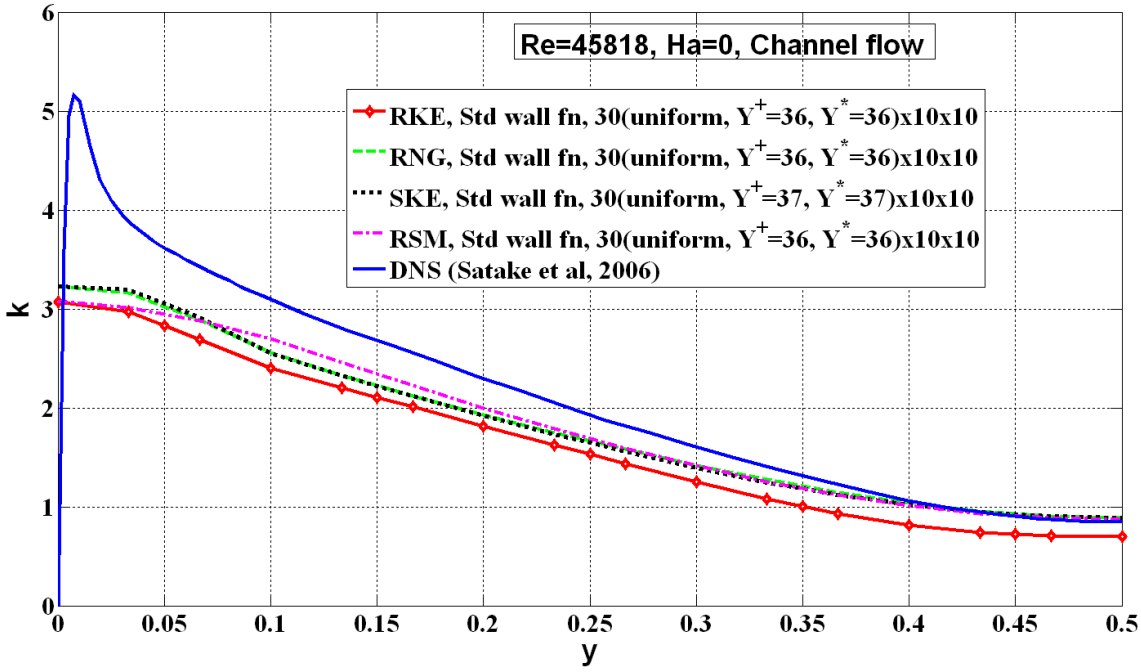

Fig-5 Comparison of TKE in various models with SWF approach in high-Re channel flow

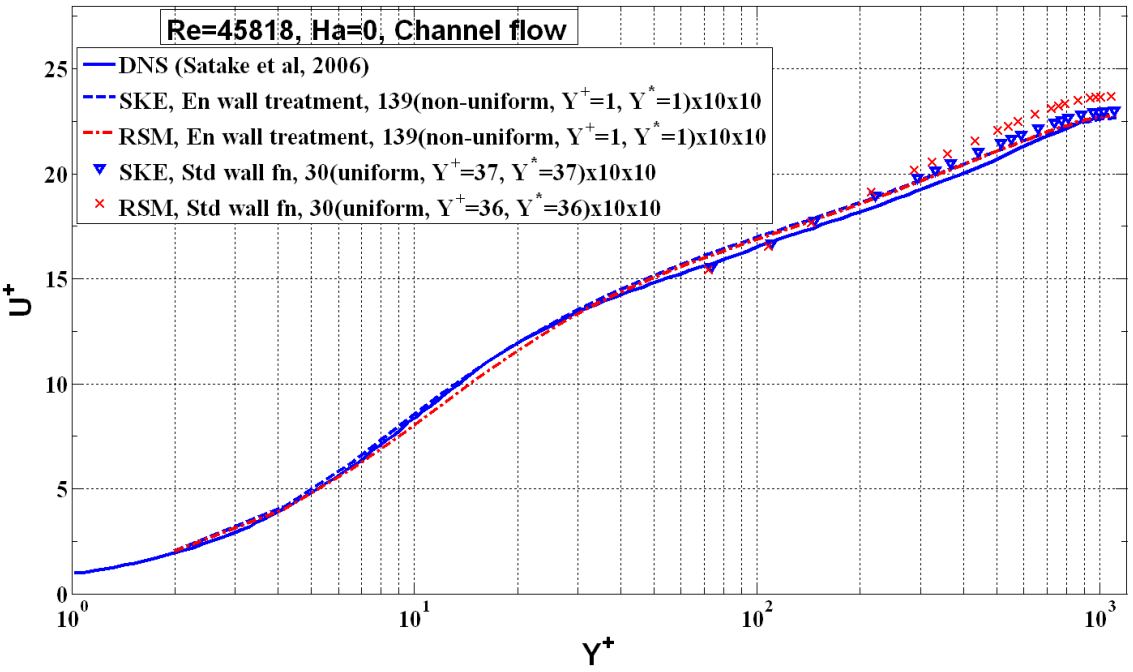

Fig-6 Comparison of normalized mean axial velocity in SKE and RSM-LPS with SWF and EWT in high-Re channel flow

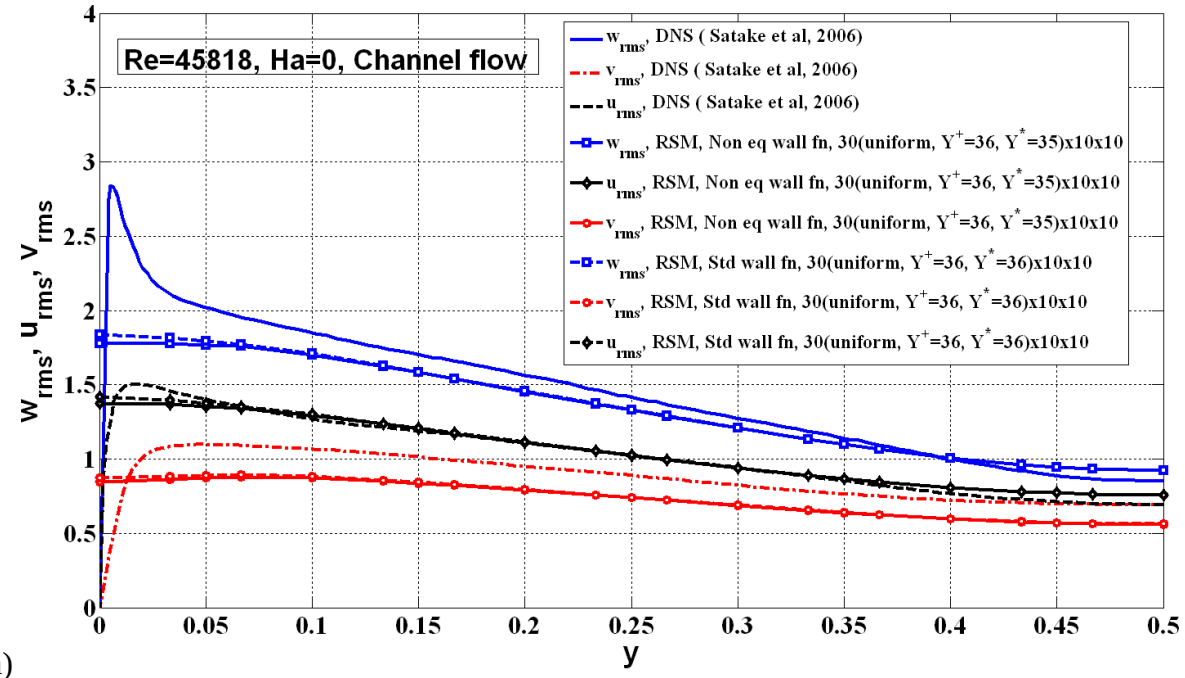

(a)

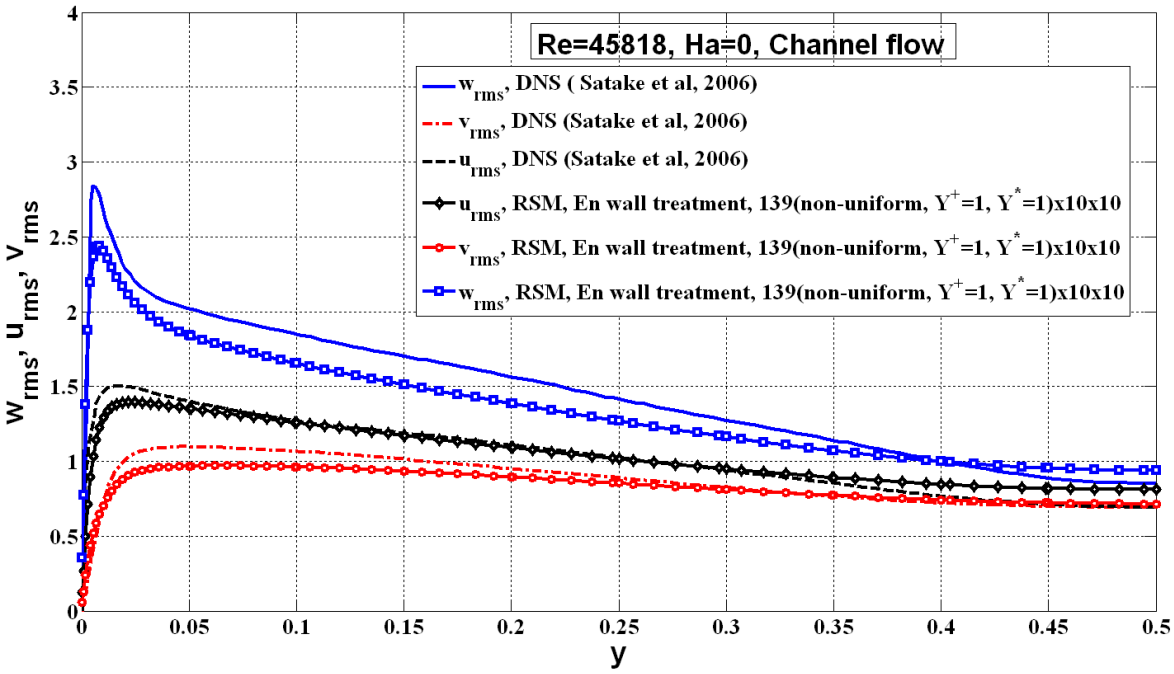

(b)

Fig-7 Comparison of RMS of velocity fluctuations in RSM-linear-pressure-strain with (a) NEWF and SWF (b) EWT in high-Re channel flow

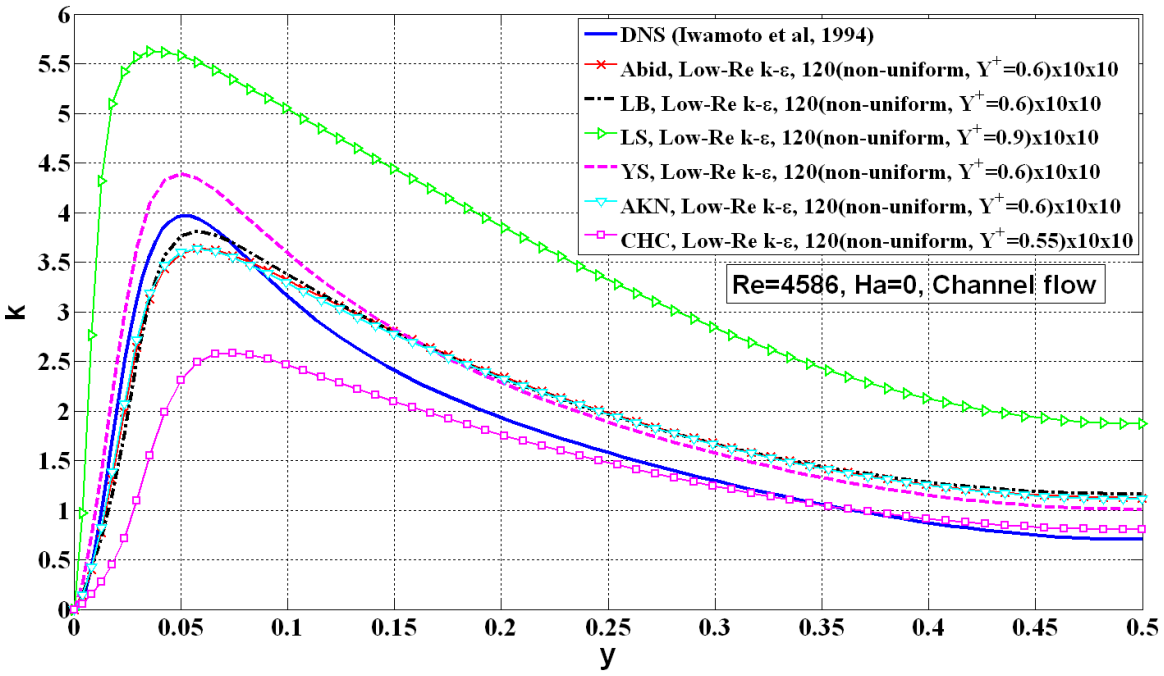

Fig-8 Comparison of TKE predicted by low-Re k-ε models with the DNS in low-Re channel flow

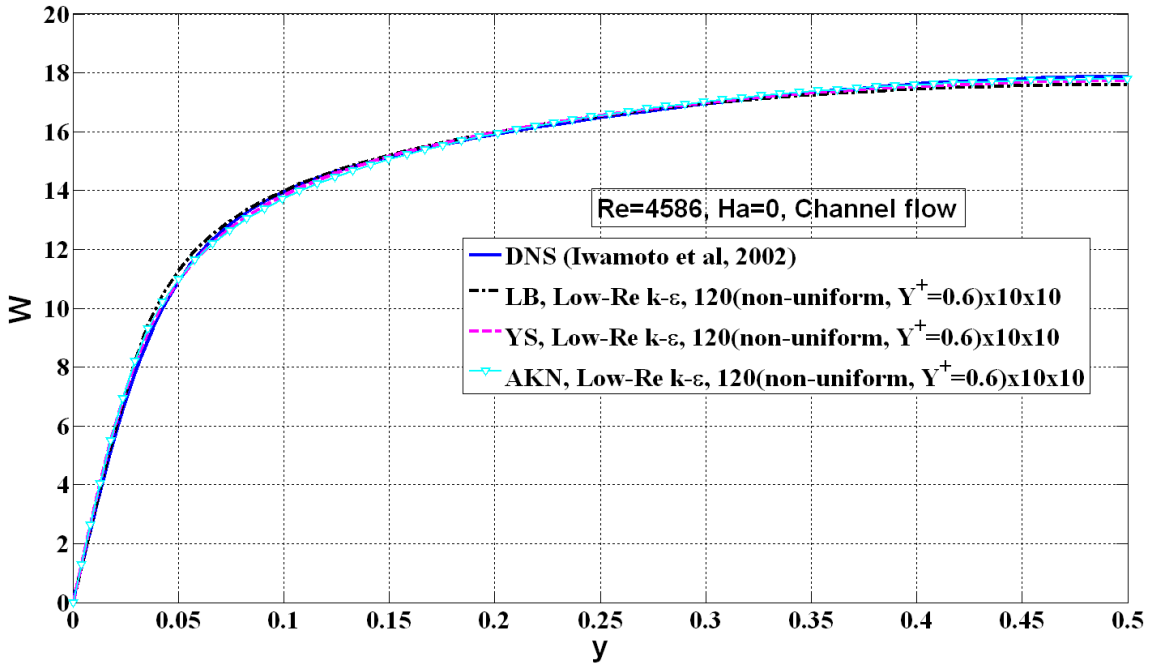

Fig-9 Comparison of the mean axial velocity predicted by low-Re k-ε models with the DNS in low-Re channel flow

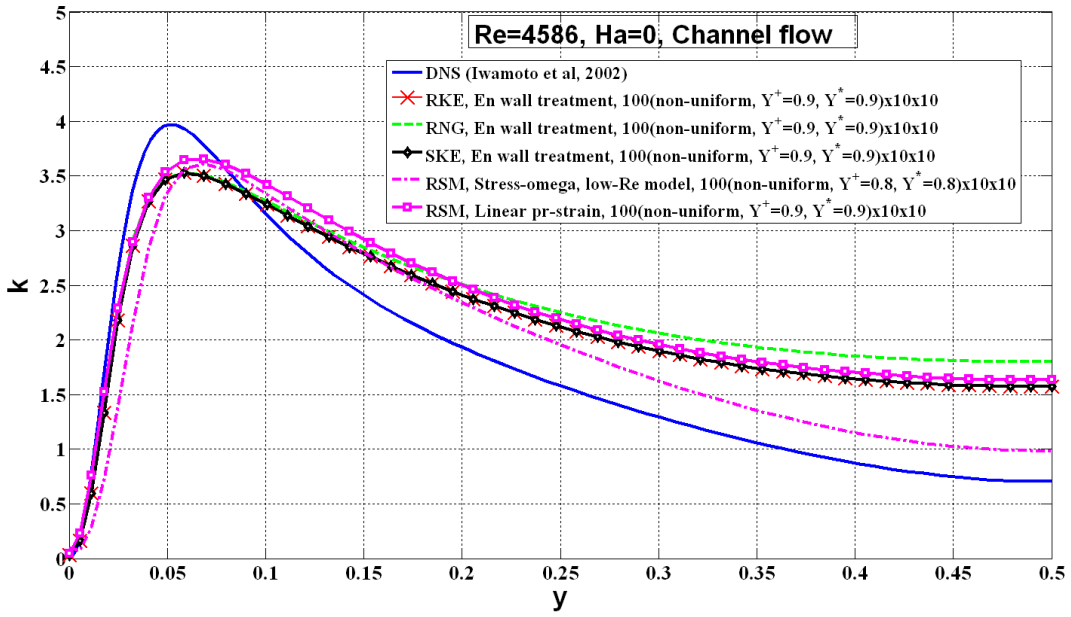

Fig-10 Comparison of TKE predicted by RKE, RNG, SKE and RSM-LPS with EWT and low-Re RSM-Sω turbulence models with the DNS in the low-Re channel flow

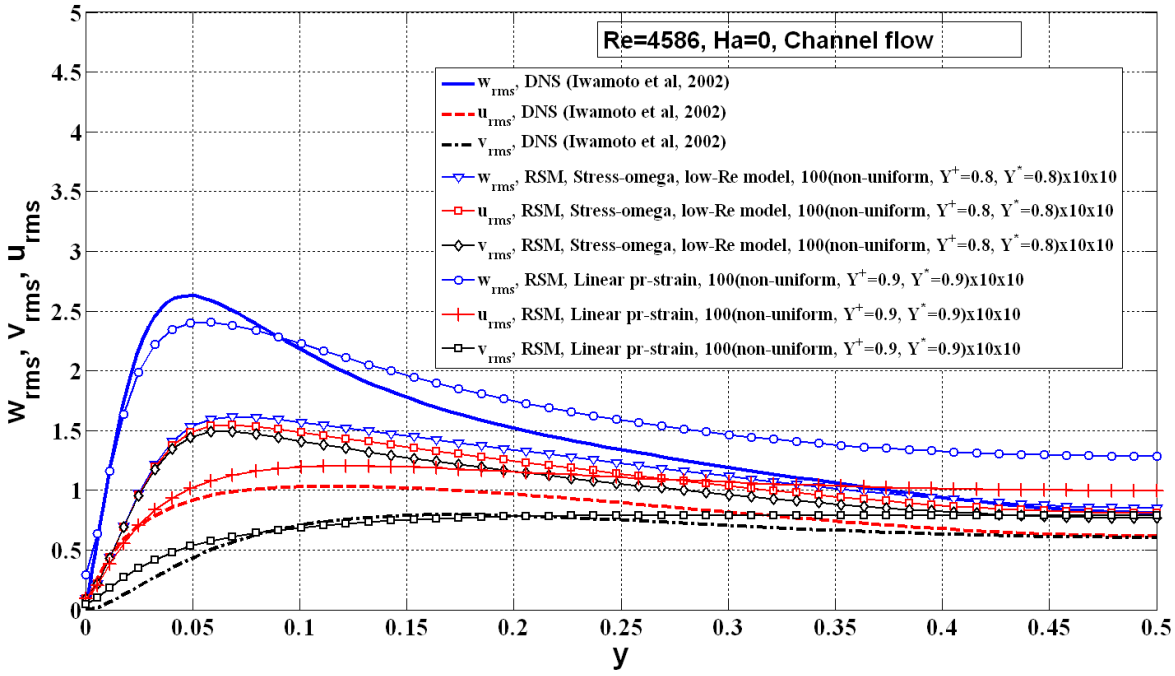

Fig-11 Comparison of RMS of velocity fluctuations by RSM models with the DNS in low-Re channel flow

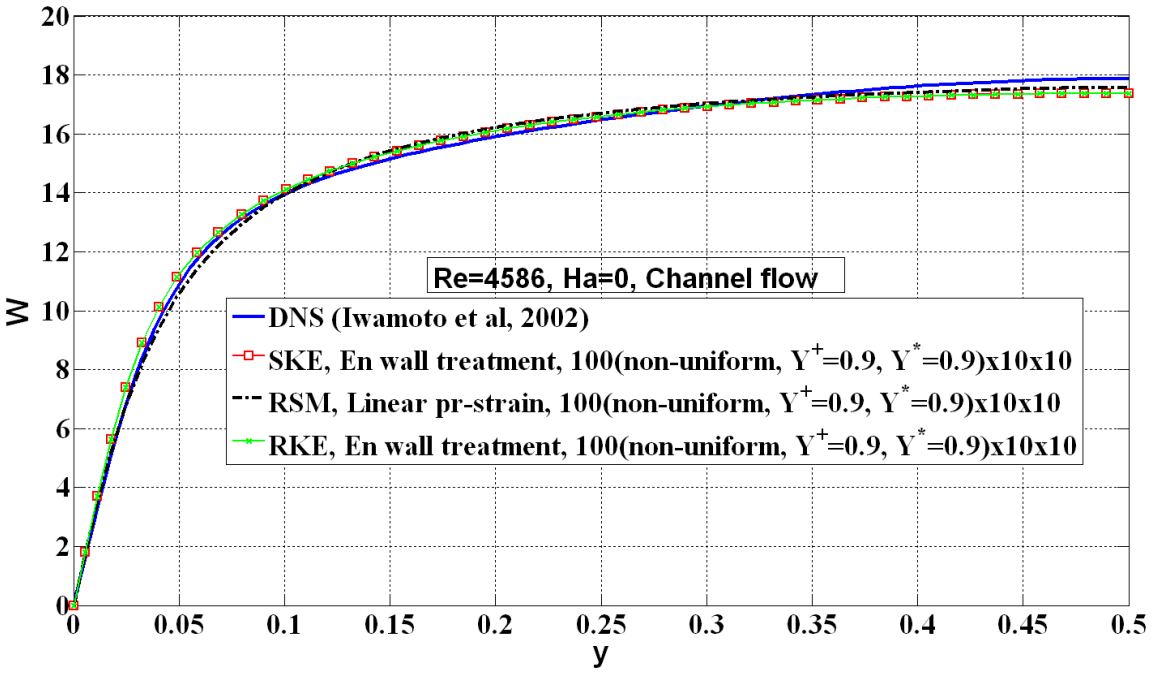

Fig-12 Comparison of mean axial velocity by SKE, RKE, RSM-LPS models with EWT with the DNS in low-Re channel flow

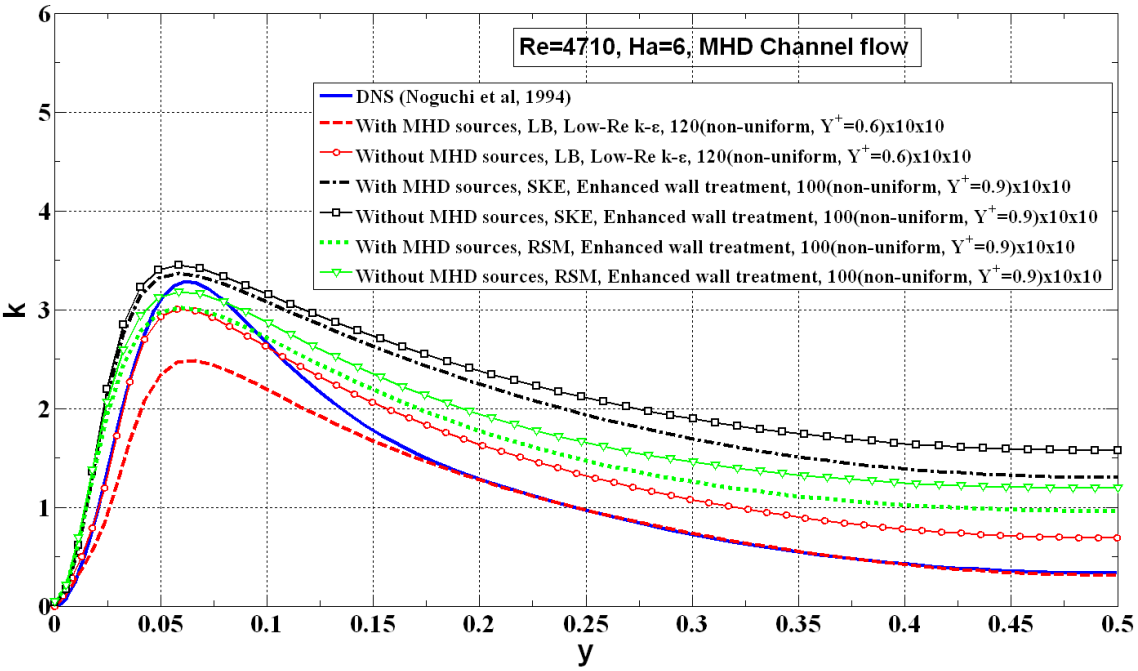

Fig-13 Comparison of TKE in low-Re MHD channel flow with various models

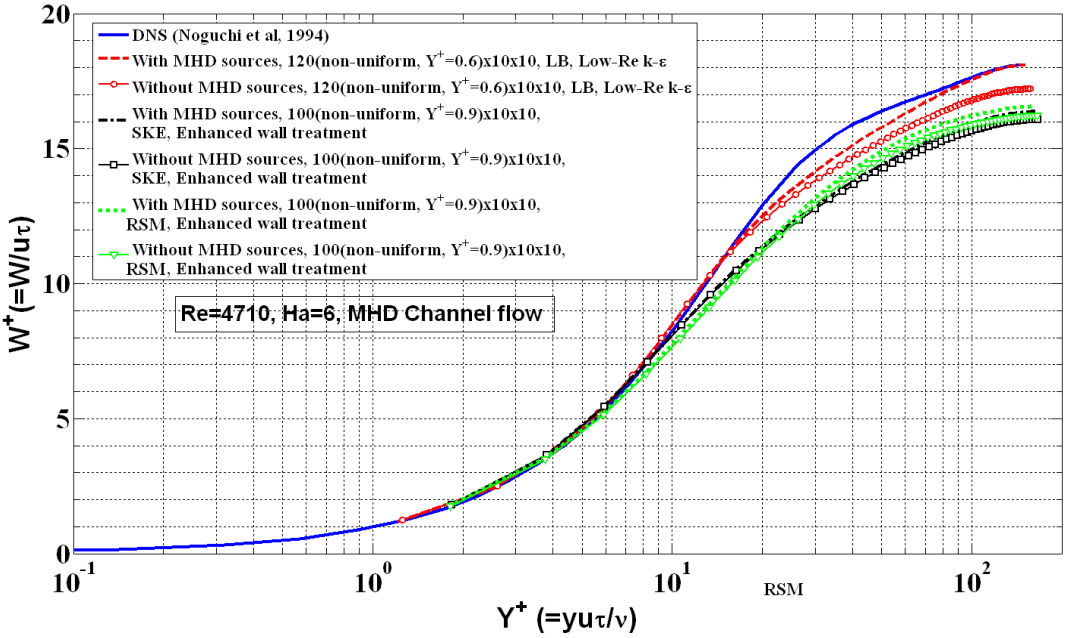

Fig-14 Comparison of normalized mean axial velocity vs. normalized wall distance in wall units in low-Re MHD channel flow in various models

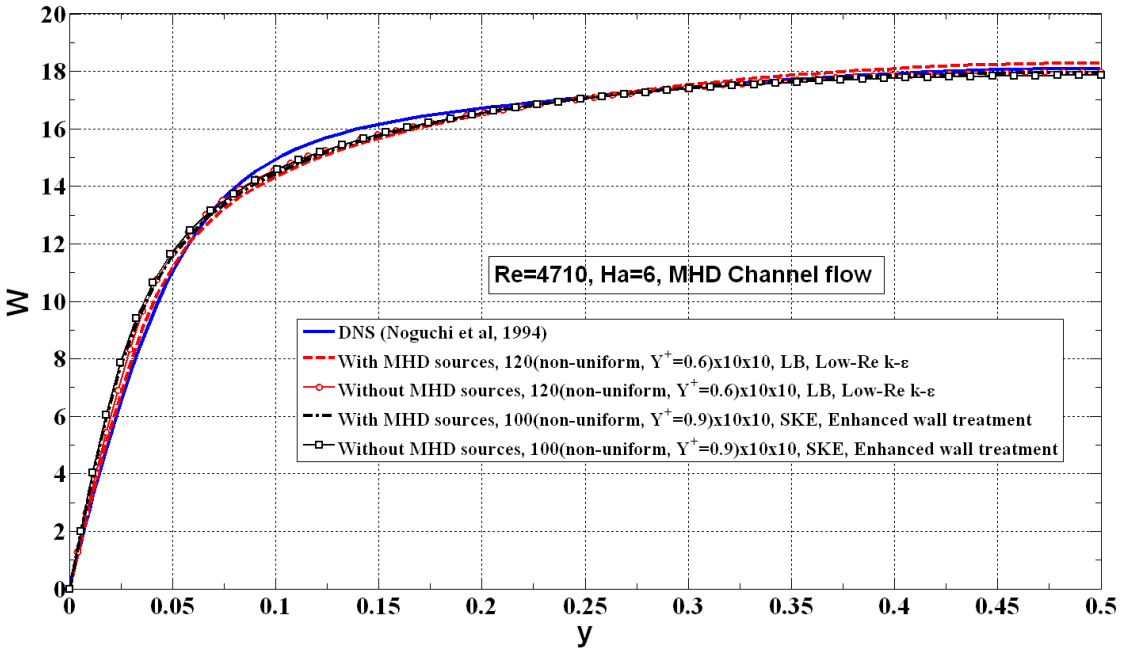

Fig-15 Comparison of mean axial velocity vs. distance from the wall in low-Re MHD channel flow in LB and SKE models

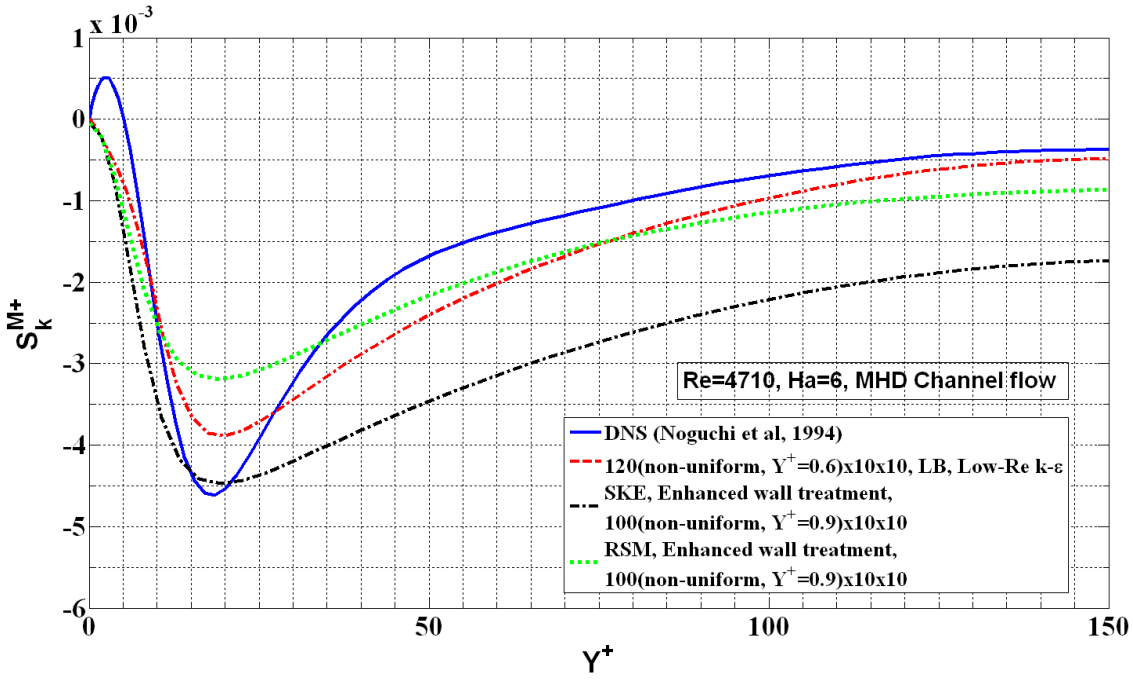

Fig-16 Comparison of the MHD source/sink in the k-equation / budget (DNS) in low-Re MHD channel flow in various models with the DNS

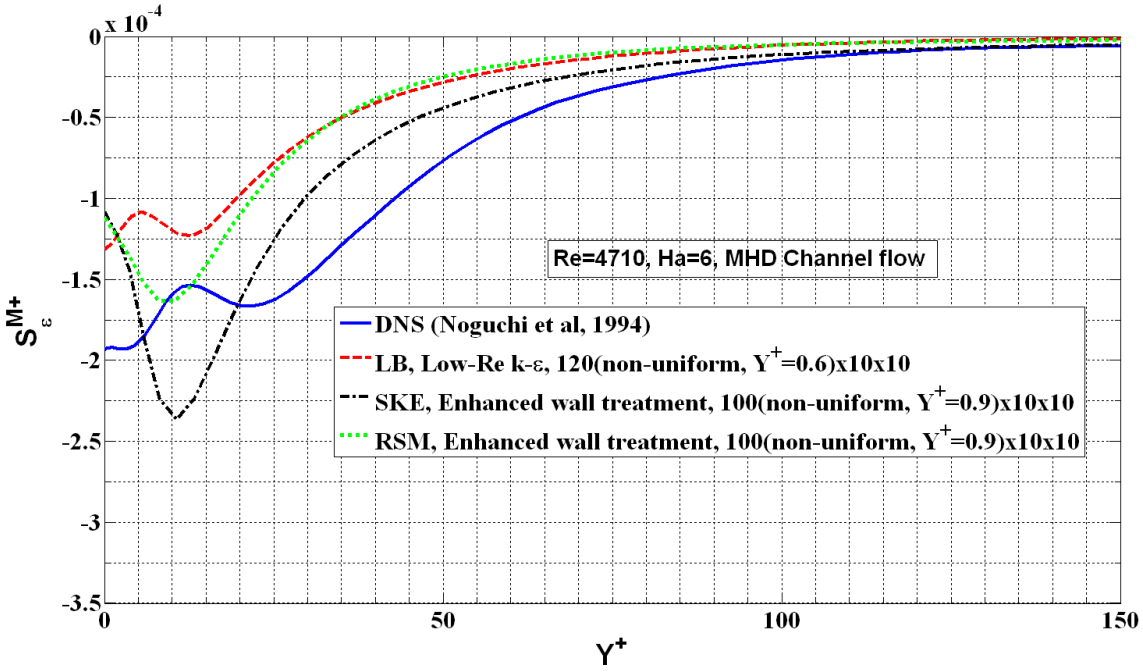

Fig-17 Comparison of MHD sink in ε-equation / budget (DNS) in low-Re MHD channel flow in various models with the DNS

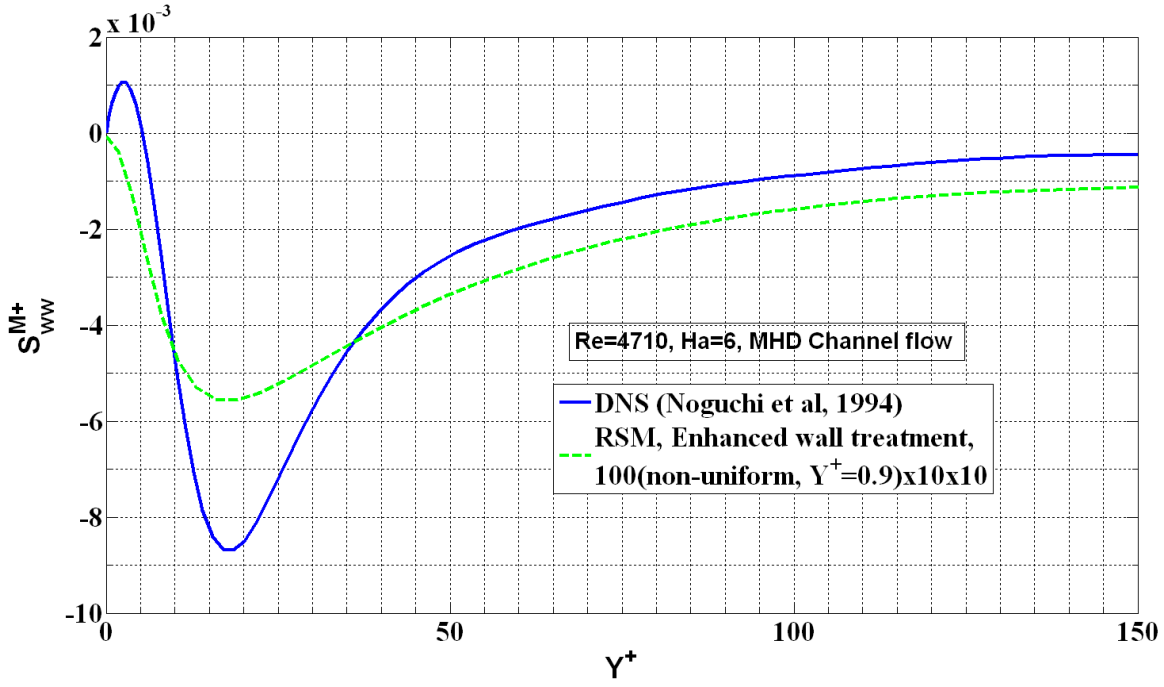

Fig-18 Comparison of the MHD source/sink in $\overline{w'w'}$-equation / budget (DNS) in low-Re MHD channel flow in RSM-LPS model with the DNS

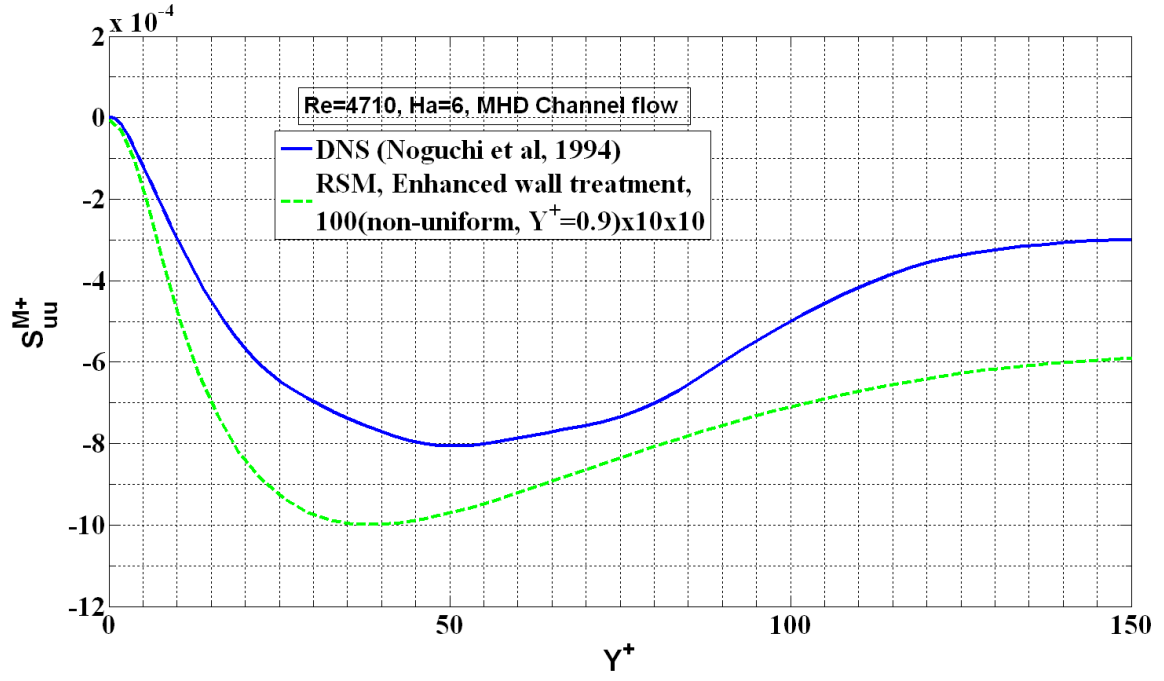

Fig-19 Comparison of MHD source/sink in $\overline{u'u'}$-equation / budget (DNS) in low-Re MHD channel flow in RSM-LPS model with DNS

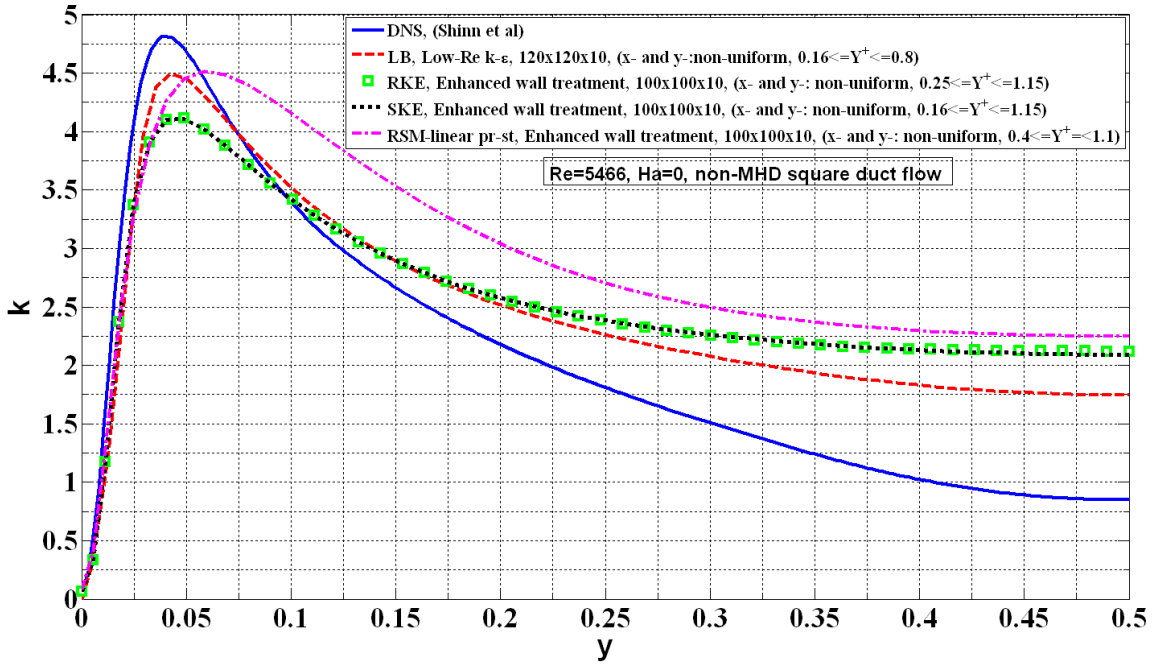

Fig-20 Comparison of TKE predicted by various models with the DNS along vertical bisector in a non-MHD square duct

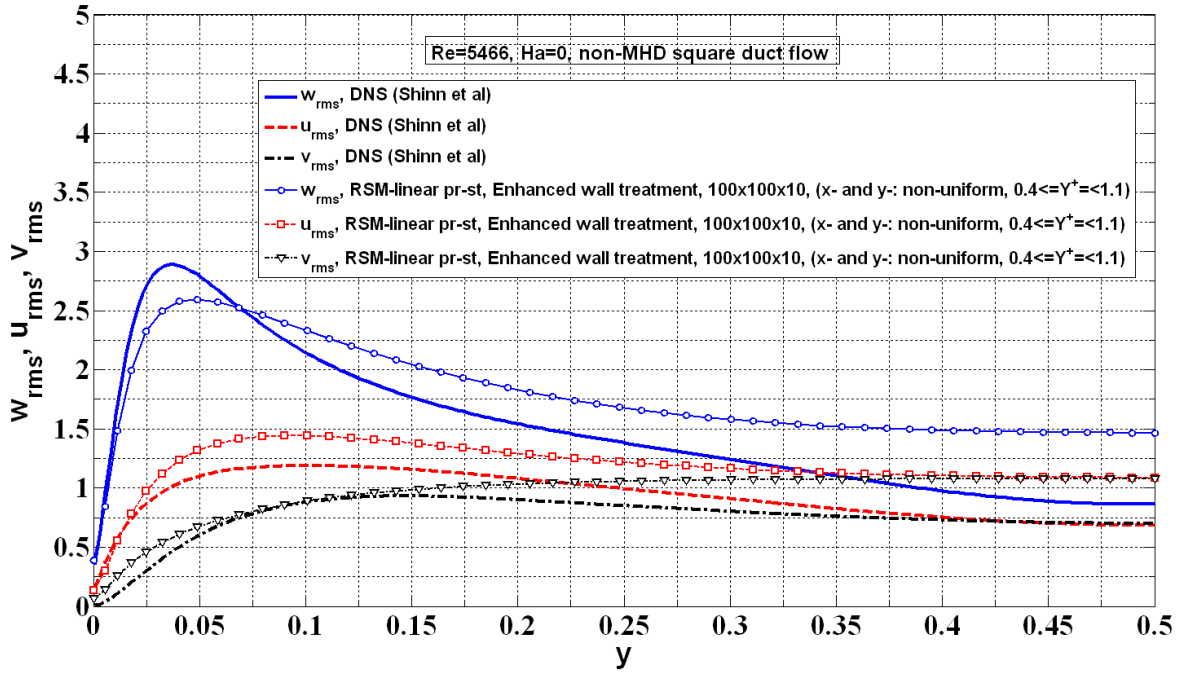

Fig-21 Comparison of RMS of velocity fluctuations predicted by RSM-LPS model with the DNS in non-MHD square duct along vertical bisector

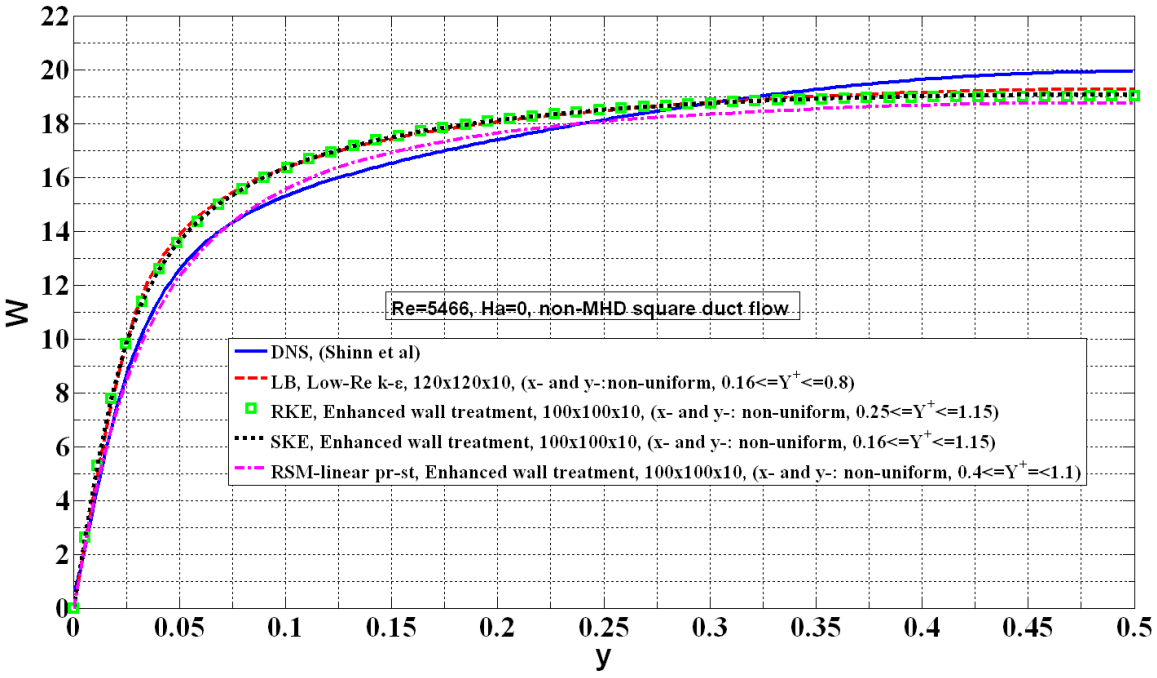

Fig-22 Comparison of mean axial velocity predicted by various models with the DNS in non-MHD square duct along vertical bisector

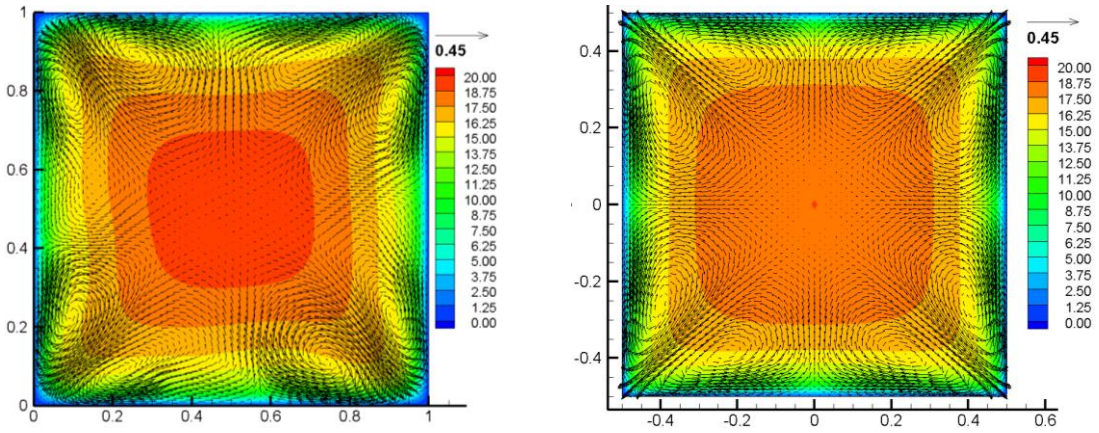

(a) DNS (Re=5466, Ha=0, Shinn et al [51]) (160x160x1024)

(b) RSM-linear-pr-strain, En wall treatment (Re=5466, Ha=0, 100x100x10)

Fig-23 Comparison of mean axial velocity contours and secondary velocity vectors in non-MHD square duct

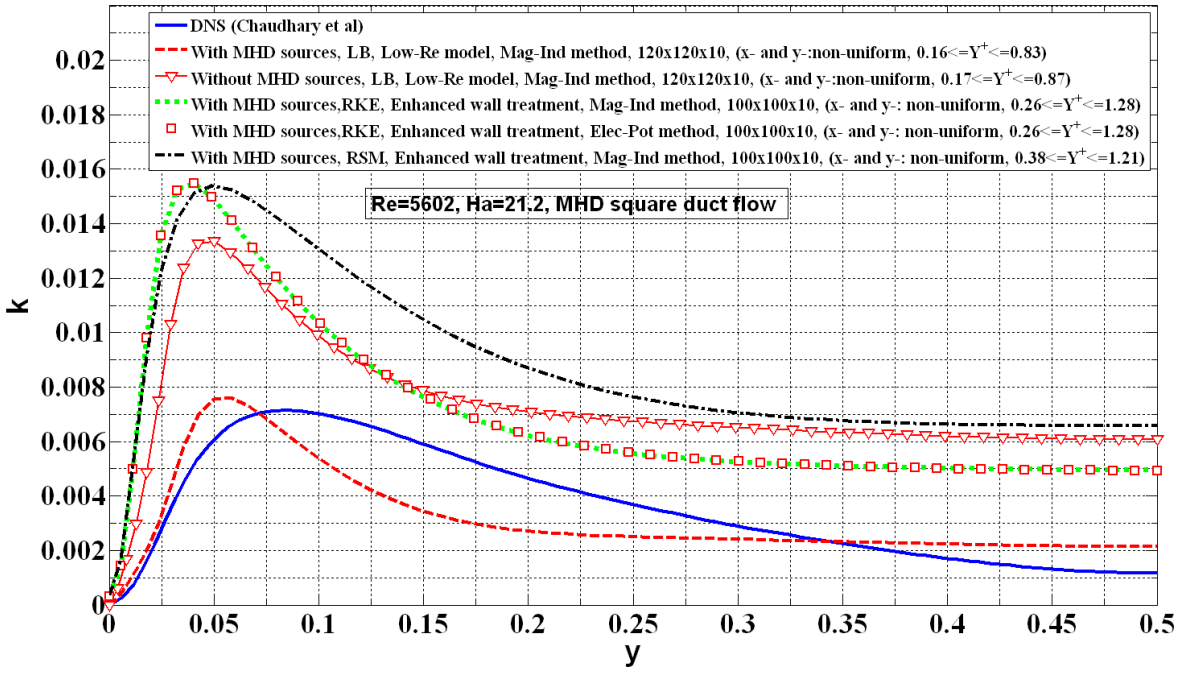

Fig-24 Comparison of TKE in various models with the DNS in MHD square duct along vertical bisector

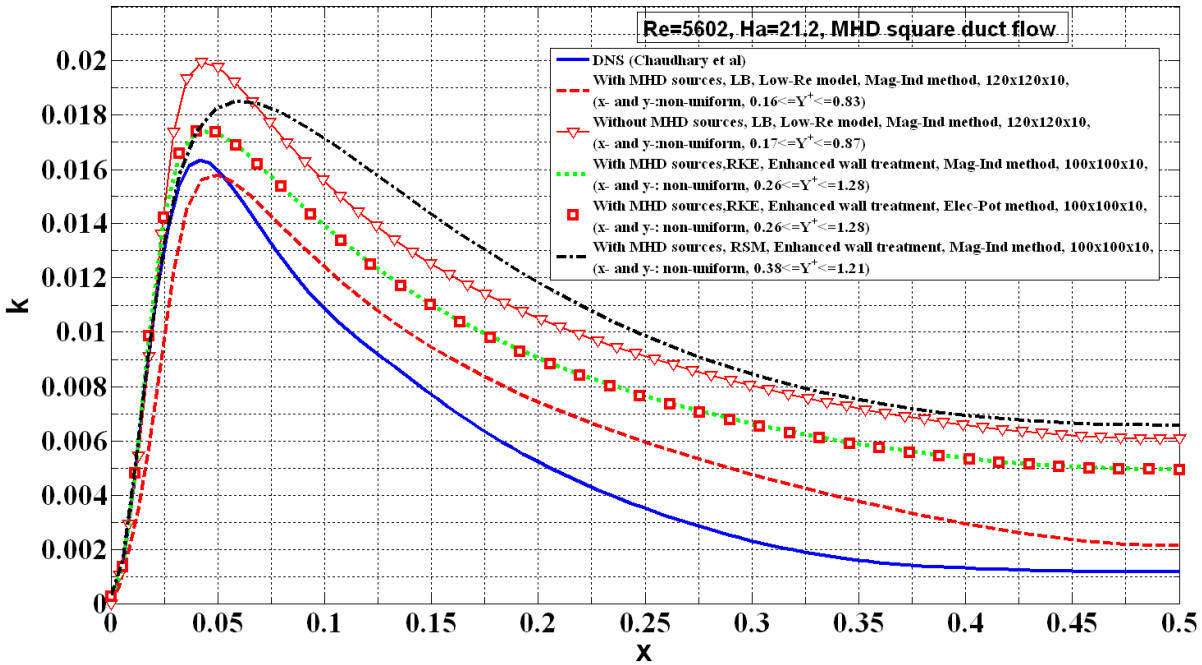

Fig-25 Comparison of TKE in various models with the DNS in MHD square duct along horizontal bisector

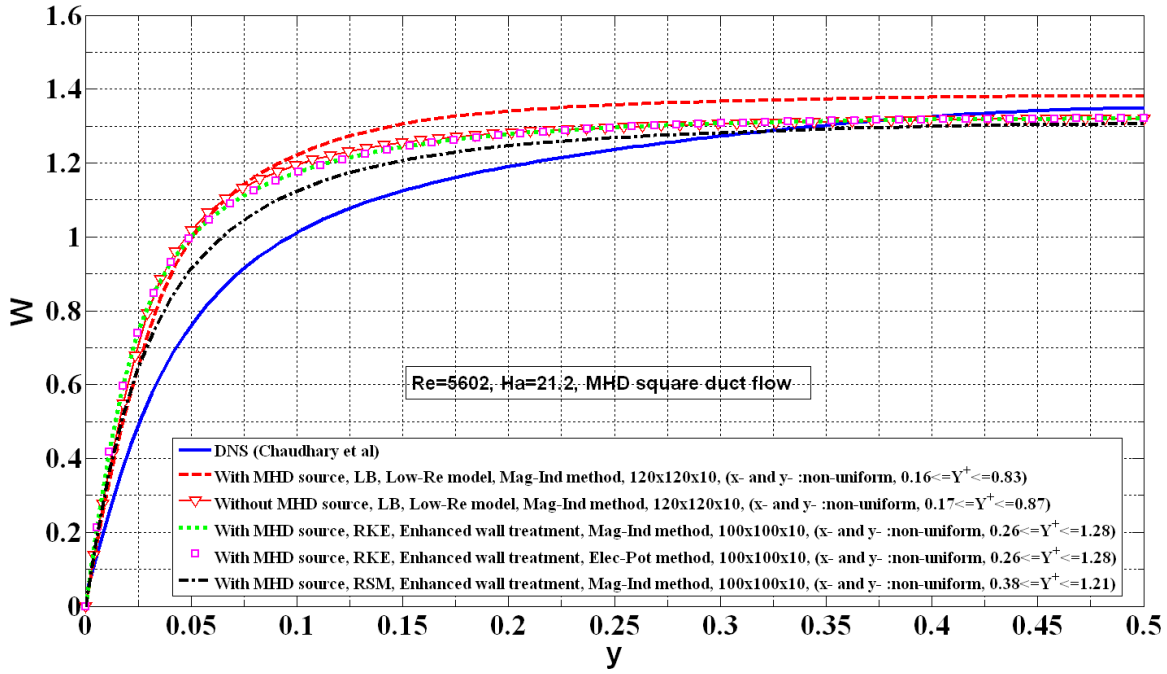

Fig-26 Comparison of the mean axial velocity predicted by various models with the DNS in MHD square duct along vertical bisector

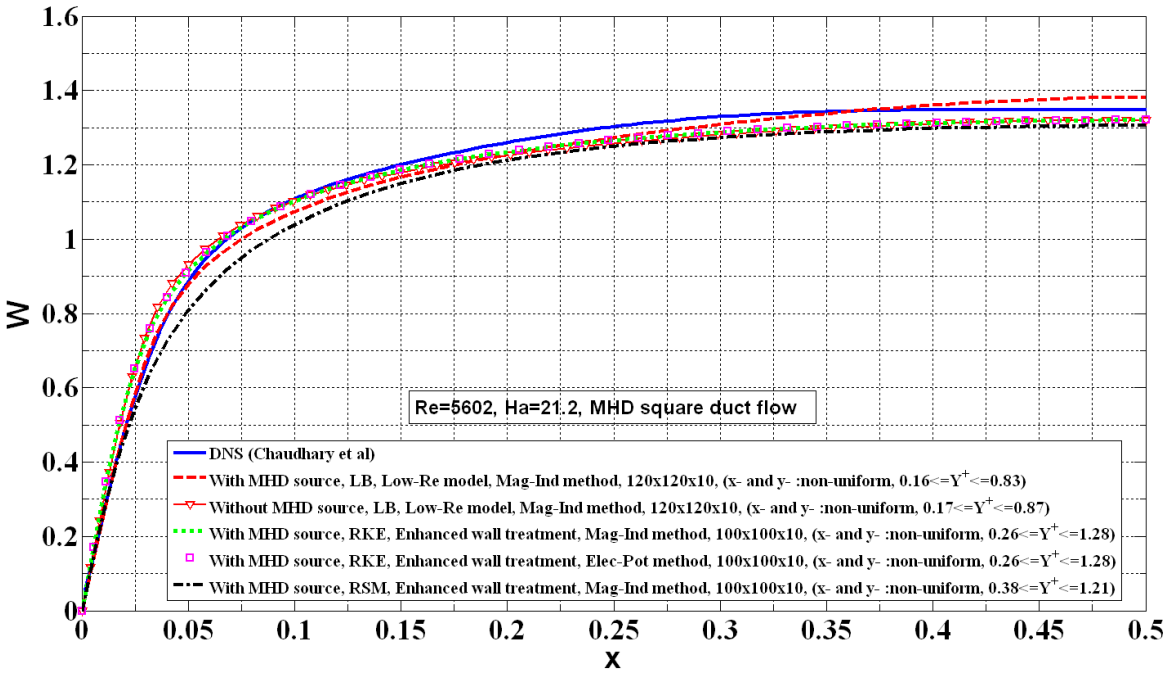

Fig-27 Comparison of mean axial velocity in various models with DNS in MHD square duct along horizontal bisector

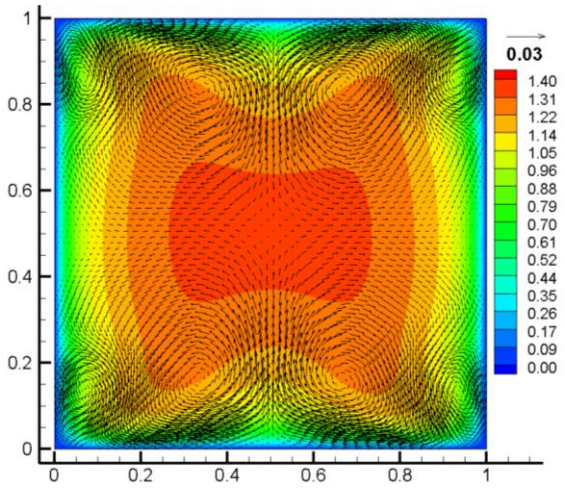

(a) DNS (Chaudhary et al [52])
(Re=5602, Ha=21.2, 128x128x512)

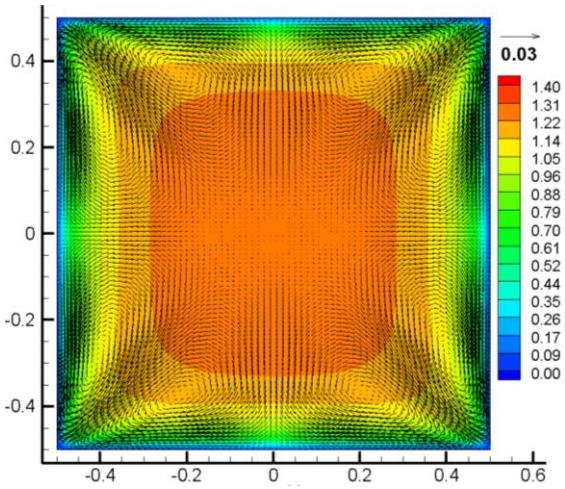

(b) RSM, En wall treatment,
Mag-Induction (Re=5602, Ha=21.2, 100x100x10)

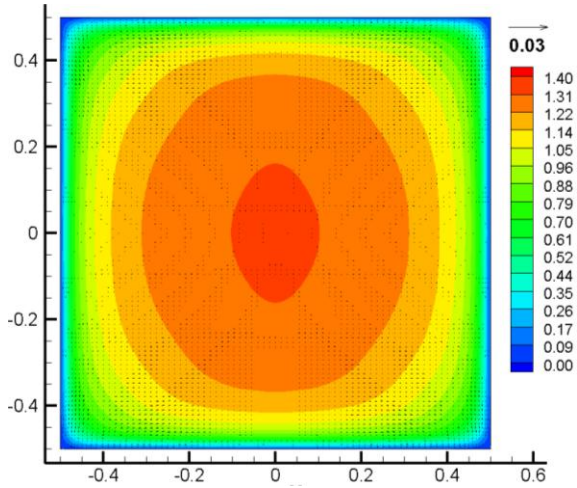

(c) Realizable k-ε, En wall treatment,
Mag-Induction (Re=5602, Ha=21.2, 100x100x10)

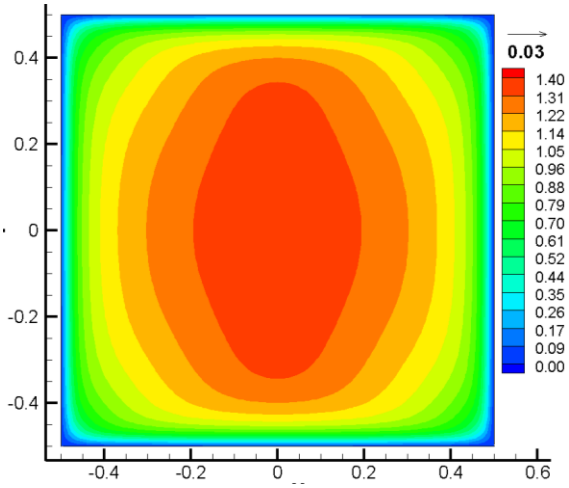

(d) LB, Low-Re k-ε,
Mag-Induction (Re=5602, Ha=21.2, 120x120x10)

Fig-28 Comparison of mean axial velocity contours and secondary velocity vectors in MHD duct

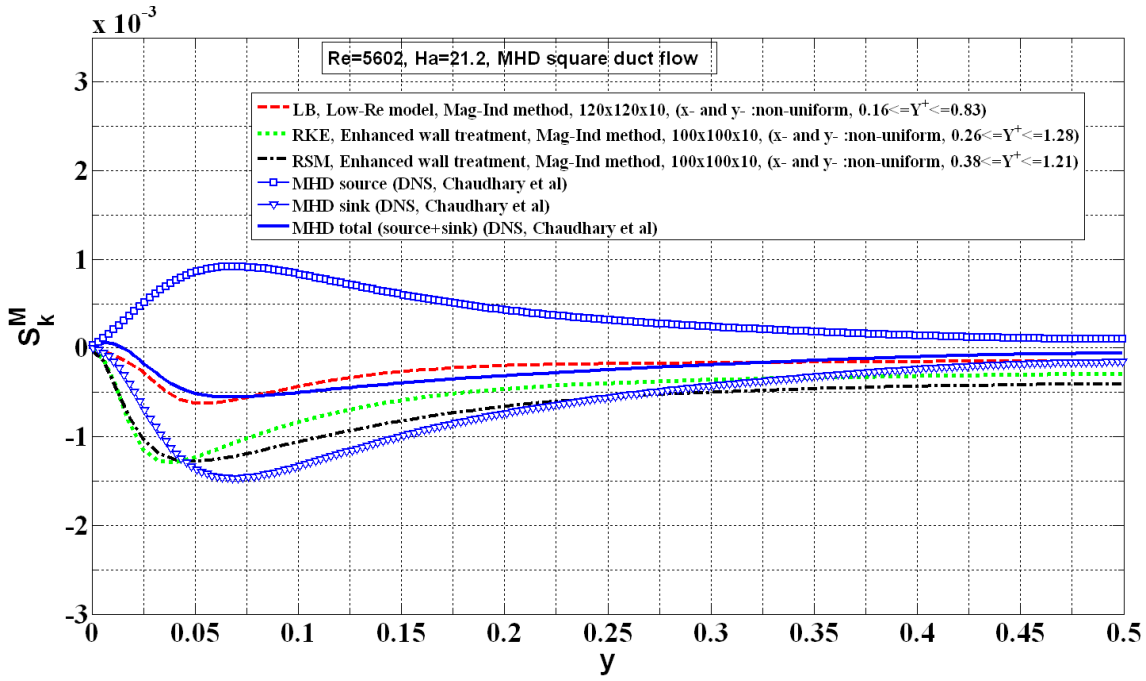

Fig-29 Comparison of MHD source/sink in k-equation / budget (DNS) predicted by various models with the DNS in MHD square duct along vertical bisector

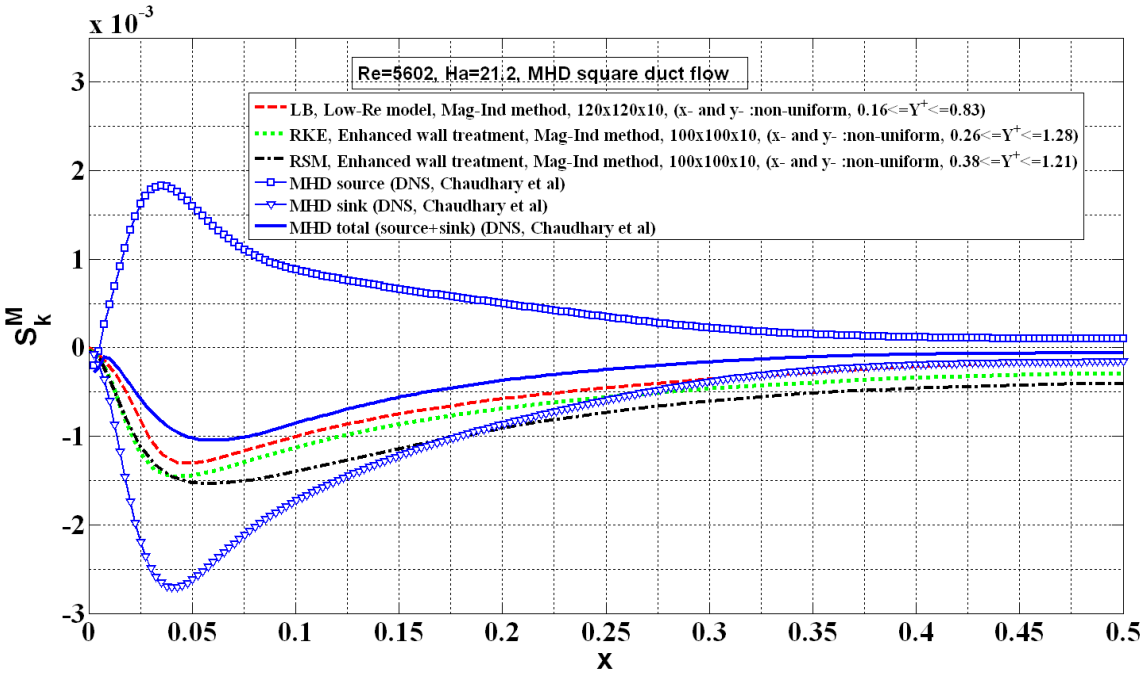

Fig-30 Comparison of MHD source/sink in k-equation / budget (DNS) in various models with the DNS in MHD square duct along horizontal bisector

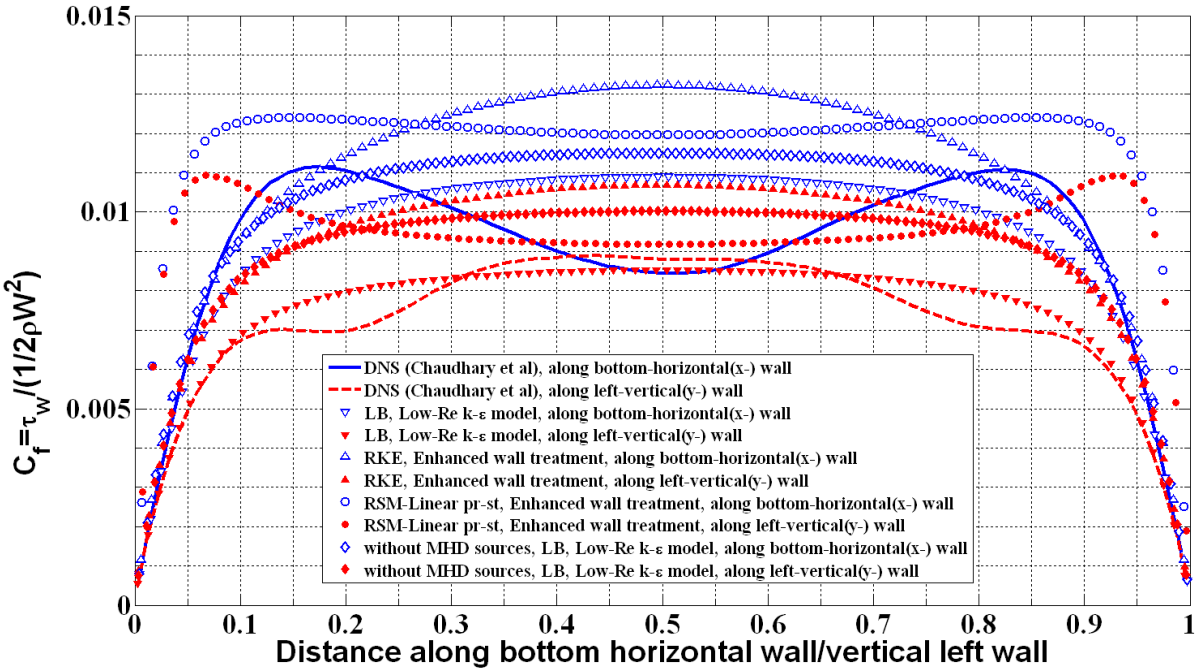

Fig-31 Comparison of the friction factor in MHD square duct along bottom-horizontal and left-vertical walls in various models with the DNS